IEEE Access
Multidisciplinary ⋮ Rapid Review ⋮ Open Access Journal

Received May 11, 2020, accepted May 22, 2020, date of publication May 26, 2020, date of current version June 8, 2020.

Digital Object Identifier 10.1109/ACCESS.2020.2997877

Neural-Networks Control for Hover to High-Speed-Level-Flight Transition of Ducted Fan UAV With Provable Stability

ZIHUAN CHENG[1], HAILONG PEI[1], (Member, IEEE), AND SHUAI LI[2], (Member, IEEE)
[1]Key Laboratory of Autonomous Systems and Networked Control, Ministry of Education, Unmanned Aerial Vehicle Systems Engineering Technology Research Center of Guangdong, South China University of Technology, Guangzhou 510640, China
[2]School of Engineering, Swansea University, Swansea SA2 8PP, U.K.

Corresponding author: Hailong Pei (auhlpei@scut.edu.cn)

This work was supported in part by the Scientific Instruments Development Program of NSFC under Grant 615278010, and in part by the Science and Technology Planning Project of Guangdong, China, under Grant 2017B010116005.

ABSTRACT In this paper, we focus on the transition control of a ducted fan vertical take-off and landing (VTOL) unmanned aerial vehicle (UAV). To achieve a steady transition from hover to high-speed flight, a neural-networks-based controller is proposed to learn the system dynamics and compensate for the tracking error between the aircraft dynamics and the desired dynamic performance. In prior, we derive the nonlinear system model of the aircraft full-envelope dynamics. Then, we propose a novel neural-networks-based control scheme and apply it on the underactuated aircraft system. Key features of the proposed controller consist of projection operator, state predictor and dynamic-formed adaptive input. It is proved and guaranteed that the tracking errors of both state predictor and neural-networks weights are upper bounded during the whole neural-networks learning procedure. The very adaptive input is formed into a dynamic structure that helps achieve a reliable fast convergence performance of the proposed controller, especially in high-frequency disturbance conditions. Consequently, the closed-loop system of the aircraft is able to track a certain trajectory with desired dynamic performance. Satisfactory results are obtained from both simulations and practical flight test in accomplishing the designed flight course.

INDEX TERMS Ducted fan, fast convergence, high-speed flight, neural networks, transition control, unmanned aerial vehicle (UAV).

I. INTRODUCTION

In recent years, vertical take-off and landing (VTOL) unmanned aerial vehicles (UAVs) have attracted more and more attentions in transportation, surveillance, detection and many other areas. Such a UAV is required to capable of VTOL, steadily hover and long-endurance high-speed flight. To meet this need, one preference is the ducted fan UAV. Ducted fan is well known for its compact layout which enables the vehicle working safely in crowed urban environments such as warehouses and alleys. During the past decades, many classical prototypes of ducted fan, like iSTAR [1], HoverEye [2] and GTSpy [3], have been invented and applied successfully. The typical configuration of a ducted fan contains one duct-fan and four control surfaces. To this layout, the fan is shrouded by a solid wall that 'ducted fan' is hence named. Comparing to a single rotor, a ducted fan features higher aerodynamic efficiency as the fan tip vortex is strongly blocked and weakened by the duct wall. Basically, fixed aerodynamic flaps and deflectable control surfaces are placed below the fan. Being exposed in the flow filed of the air exhausted from the fan, the fixed flaps collectively generate an anti-torque moment counteracting the fan torque, while the control surfaces create attitude control moments. Similar to a helicopter or a quadrotor, this typical configuration results in an underactuated property of the ducted fan dynamic system.

One important characteristic that distinguishes ducted fan from rotorcraft is the high-speed level flight capacity. Notice that, for rotorcrafts like helicopters or quadrotors, flying at high-speed (>10m/s) requires a large pitching angle of the rotor disc, which results in more power consumption than hover. Thus, this high-speed flying status is generally

The associate editor coordinating the review of this manuscript and approving it for publication was Jiankang Zhang.

This work is licensed under a Creative Commons Attribution 4.0 License. For more information, see https://creativecommons.org/licenses/by/4.0/

considered as transient maneuvering for these rotorcrafts, not an economical working point. On the contrary, when flying horizontally at high-speed, a ducted fan is subject to an aerodynamic lift which is considerably larger than the associated drag. It is hence indicated that the power consumption in this high-speed-level-flight condition is less than that in hover. This special aerodynamic property can remain effective on a single duct-and-fan structure, even without a wing. Therefore, similar to a fixed-wing airplane, a ducted fan is capable of conducting long-distance missions with high-speed economical cruising. For instance, to the ducted fan studied in this paper, the power rate of steady flight at 20m/s is less than 1/3 of that in hover, and the aircraft is functioned of 15min hovering or 27km flight radius (54km maximum range).

It is of great significance to study the transition control for hover to high-speed flight of ducted fan UAV. Till now, most previous works on this aircraft are concentrated on *near-hover* and *low-forward-speed* control. At near-hover point, the aircraft dynamics can be simplified into linear system with underactuated property [4]. In [5], a cascade PID controller is designed to achieve good performance in simulation. More complex control structures are adopted to handle the nonlinearity with good performance in practice [6], [7]. Taking consideration of uncertainty and disturbance, adaptive control schemes [8]–[10] are proposed for better control accuracy and disturbance rejection performance. However, it is challenging to design a proper controller for the hover to high-speed transition process. On one hand, as the relevant system values suffer great changes from hover to level flight, the equilibrium point of the aircraft dynamic system encounters a considerable deviation with highly nonlinearity. On the other hand, as the forward speed increases, the aerodynamic effects on the control surfaces are enhanced and the aircraft becomes more and more sensitive to input noises as well as relevant disturbances.

Till now, this transition control is mostly studied for tail-sitter VTOL UAV. In [11], [12], a ducted-fan-pushed fixed-wing tail-sitter UAV is studied. An L1 adaptive controller is applied on its transition control based on linearized model. In [13], a vectored-thrust tail-sitter UAV is studied, the system model of which is to an extent similar to the ducted fan. In this work, a robust controller is proposed to tackle the complexity of aerodynamic effects and conduct the transition process. In contrast to a typical tail-sitter configuration, a ducted fan without a wing features highly aerodynamic coupling and unstable properties. Thus, for the transition control of a ducted fan UAV, it is essential to deal with the nonlinearity and uncertainty of the aircraft system. Neural networks (NNs) have been widely employed to aircraft control for its excellent performance in nonlinearity matching and uncertainty compensation [14]–[18]. In [19], NNs are introduced to learn the uncertainties online and control a small quadrotor. In [20], a NNs based robust adaptive controller is proposed to identify the inertia matrix of a small helicopter. In [21], NNs are introduced to enhance the performance of a dynamic inversion control scheme.

Another important issue taken into account is the feasibility for implementing the designed controller. In terms of controller design of a rotorcraft, a cascade PID controller is widely used for its convenient in practical parameter tuning at hover. However, controller design for a fixed-wing at high-speed flight takes much more efforts. Generally, taking safety into consideration, the parameters of this controller are directly tuned on the real aircraft in a wind tunnel, or pre-tuned on a mathematical model which is acquired through wind tunnel tests or computational fluid dynamics (CFD). Unfortunately, all of these methods are complicated and costly on both money and time. Therefore, the basic idea for the proposed controller in this paper is to build a reference system, which is easy to tuned such as cascade PD controller, and use NNs to learn and compensate for all the uncertainties between the real system and the reference system. This control structure is of great advantage in practical implementation.

One core objective for NNs design is fast convergence of the weights and reconstruction errors. In [22], an experience replay based learning algorithm is proposed to obtain fast learning performance with estimation error uniformly ultimately bounded (UUB). However, the UUB property cannot guarantee the transient performance in the early stage of parameter adaptation. In [23], a neural learning controller is proposed to improve this transient performance on controlling marine surface vessels. In order to achieve high tracking accuracy with fast uncertainty matching, a state predictor is introduced into the control scheme in [24], in which the NNs update from both tracking error and prediction error. Generally, enlarging the learning rate of the weights contributes to the increasing of estimation convergence rate of NNs. But this may also lead to great system oscillation or even an overshoot problem in the early adaptation process. To deal with this issue, projection operator is invoked into the weights-tuning law that constrains the NNs weights into certain compact sets. As a result, the NNs with projection operator show excellent performance in the reconstruction of time-varying disturbance and uncertainties [25]–[28].

Based on the concerns above, we propose a novel neural-networks-based control scheme. The controller is constructed to track a reference system with tracking error learned and compensated by NNs. Projection operators and state predictors are introduced into the NNs learning algorithm to achieve fast convergence performance. Additionally, we design an adaptive control law with a dynamic form to enhance the robustness of the closed-loop system. To show the advantage of the proposed method, a comparison between the proposed controller and standard approaches is given in Table 1.

In this paper, we study the transition control of a small ducted fan UAV with the typical one duct-fan and four control surfaces layout (See Fig.1 and Fig.2.). Additionally, the aircraft is installed with an extra front wing for balancing the

TABLE 1. Comparison between the proposed controller and standard approaches.

Control approach	Knowledge of the plant system	Performance in complex nonlinear structure	Robustness	Implementation for aircraft systems
PID	Not required	Not guaranteed	acceptable	easy
Adaptive	Partly required	Depend on the structural knowledge of the system	Bad in high adaptation rates	hard
Robust	Partly required	Depend on the knowledge of the bounds of uncertainty	good	hard
Proposed NNs	Not required	Guaranteed	good	easy

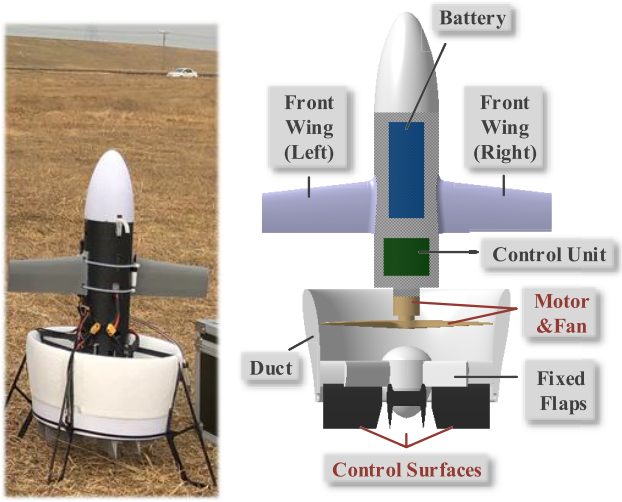

FIGURE 1. The ducted fan studied in this paper and its layout.

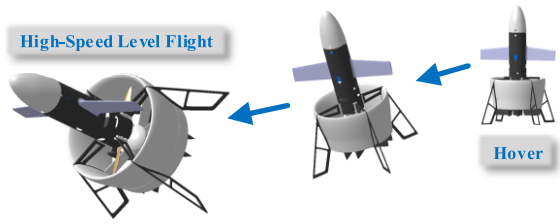

FIGURE 2. Illustration of the hover to high-speed-level flight transition process.

pitching moment. We first analyze the aerodynamic characteristics of the ducted fan model during the hover to high-speed transition process. Then a novel neural-networks-based control scheme for nonlinear system is proposed. Based on these, a cascade flight control strategy is designed for the transition control of the ducted fan UAV. The paper is organized as follows: the aerodynamic analysis and system modeling of the ducted fan studied in this paper are presented in Section II. In Section III, a neural-networks-based controller for nonlinear system is proposed with a nominal design and its proof of stability. In Section IV, based on the proposed NN controller, a cascade flight strategy is designed for the aircraft to track certain reference inputs with desired dynamic performance. Then simulations and flight test results are respectively shown in Section V and Section VI. Finally, Section VII draws the main conclusion.

The main contributions of this paper are summarized as follows:

1) A novel neural-networks-based control scheme for nonlinear system is proposed. To track a reference system, NNs and adaptive control law are designed to eliminate the tracking error between the original system and the reference system. With the introduction of projection operators, state predictors and high-order adaptive control law, the closed-loop system achieves a good robustness with fast convergence of the NN weights. The stability of the proposed controller is theoretically proved.
2) The proposed NNs control scheme is successfully applied on the transition control of a ducted fan UAV. Both simulation and practical flight test results verify the effectiveness and reliability of the proposed method. Additionally, we give a comparison result between the proposed method and an adaptive method mentioned in [29] in order to reveal the advantage of the proposed method.

II. AIRCRAFT SYSTEM MODELING

In this section, the 6 degree-of-freedom (DOF) motion dynamics of the ducted fan is derived from Newton and Euler Theorems. Then corresponding aerodynamic characteristics are presented and analyzed particularly for the transition process. Although neural-networks control is usually model free, a precise and reliable mathematical model is necessary and contributes to the follows:

- To make the simulations more convincible and help choose the proper basis functions of the proposed NNs.
- To deeply indicate the advantage of using neural-networks by showing the complexity of the system model in transition.

A. 6-DOF KINEMATICS

Basically, we describe the 6-DOF motion of a rigid body by adopting two reference frames in Cartesian coordinates. $\{X_E, Y_E, Z_E\}$ denotes the inertial frame defined by north-east-down. $\{X_b, Y_b, Z_b\}$ denotes the body frame attached to the aircraft. Position in the inertial frame is denoted as $\mathbf{p} = [x \;\; y \;\; z]^T$. Velocity in the inertial frame and the body

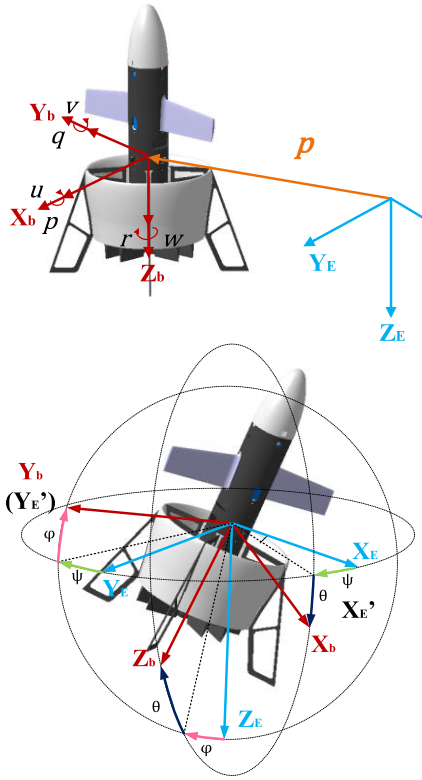

FIGURE 3. Definitions of coordinates and state variables.

frame are respectively denoted as $\mathbf{V}_E = [V_{xE} \;\; V_{yE} \;\; V_{zE}]^T$ and $\mathbf{V}_b = [u \;\; v \;\; w]^T$. In this paper, we adopt Euler angles $\boldsymbol{\xi} = [\varphi \;\; \theta \;\; \psi]^T$ to describe the aircraft attitude with 'ZXY' rotation order (See Fig.3). $\boldsymbol{\omega} = [p \;\; q \;\; r]^T$ denotes the angular velocity with respect to the body frame. Based on the 'ZXY' rotation order, rotation matrix $\mathbf{R}$ from body frame to inertial frame and the derivatives of Euler angles are given by:

$$\begin{aligned}
\mathbf{R} &= \begin{bmatrix} C\psi C\varphi & -S\psi C\theta + C\psi S\varphi S\theta & S\psi S\theta + C\psi S\varphi C\theta \\ S\psi C\varphi & C\psi C\theta + S\psi S\varphi S\theta & -C\psi S\theta + S\psi S\varphi C\theta \\ -S\varphi & C\varphi S\theta & C\varphi C\theta \end{bmatrix} \\
\dot{\xi} &= \mathbf{Q}\omega \\
\mathbf{Q} &= \begin{bmatrix} C\theta & 0 & -S\theta \\ S\theta T\varphi & 1 & C\theta T\varphi \\ S\theta/C\varphi & 0 & C\theta/C\varphi \end{bmatrix}
\end{aligned} \tag{1}$$

where C, S, and T respectively denote cosine, sine and tangent functions for short.

Remark 1: In this paper, we adopt 'ZXY' rotation order to define Euler angles rather than 'ZYX' which is common-used in attitude description. During the transition, since the aircraft pitches and the roll angle φ is around zero, $\mathbf{Q}$ defined by (1) is always invertible and far away from singularity (i.e. $\varphi = 90°$). This helps prevent the *gimbal lock* problem of a tail sitter UAV.

Velocity of environmental wind disturbance is denoted as $\mathbf{D}_w = [D_x(t) \;\; D_y(t) \;\; D_z(t)]^T$ in the body frame. Subsequently, we define airspeed V_w, angle of attack (AOA) α and sideslip angle β by:

$$\begin{aligned}
V_w &= \sqrt{(u - D_x)^2 + (v - D_y)^2 + (w - D_z)^2} \\
\cos\alpha &= -(w - D_z)/V_w, \quad 0 \le \alpha \le \pi \\
\tan\beta &= (v - D_y)/(u - D_x), \quad -\frac{\pi}{2} \le \beta \le \frac{\pi}{2}
\end{aligned} \tag{2}$$

$\mathbf{F}$ and $\mathbf{M}$ respectively denote the resultant force and moment, exclusive of gravity, in the body frame:

$$\begin{aligned}
\mathbf{F} &= \mathbf{F}_T + \mathbf{F}_m + \mathbf{F}_d + \mathbf{F}_w \\
\mathbf{M} &= \mathbf{M}_{fan} + \mathbf{M}_{cs} + \mathbf{M}_f + \mathbf{M}_g + \mathbf{M}_d + \mathbf{M}_w
\end{aligned} \tag{3}$$

where all the components are discussed below.

The fan is generally regarded as a disc acting a steady thrust and torque on the aircraft. Hence, according to *Newton and Euler's Law of Motion*, the dynamics of the aircraft is derived as follows:

$$\begin{cases}
\dot{\mathbf{p}} = \mathbf{V}_E \\
\dot{\mathbf{V}}_E = \frac{1}{m}\mathbf{R}\mathbf{F} + \begin{bmatrix} 0 & 0 & g \end{bmatrix}^T \\
\dot{\xi} = \mathbf{Q}\omega \\
\dot{\omega} = \mathbf{J}^{-1}\left[\mathbf{M} + \mathbf{J}\omega sk(\boldsymbol{\omega})\right]
\end{cases} \tag{4}$$

where m denotes the mass and $\mathbf{J} = diag(J_x, J_y, J_z)$ denotes the inertia matrix of the aircraft. g denotes the gravity acceleration. 'sk' denotes the skew symmetric matrix to a vector. The relevant definition in $\mathbb{R}^3$ is given by:

$$sk(\mathbf{x}) = \begin{bmatrix} 0 & -x_3 & x_2 \\ x_3 & 0 & -x_1 \\ -x_2 & x_1 & 0 \end{bmatrix}$$

B. AERODYNAMIC CHARACTERISTICS

Basically, as a special type of tail-sitter VTOL aircraft, a ducted fan features the same as a rotorcraft at hover or vertical flight, and acts more like a fixed-wing airplane when levelly flying with high-speed [30], [31]. In this part, we give the detailed expressions of all the forces and moments in (3).

1) DRIVING FORCE AND MOMENT

Thrust $\mathbf{F}_T$ is regarded as the driving force of the aircraft that can be expressed as:

$$\begin{cases}
\mathbf{F}_T = \begin{bmatrix} 0 & 0 & -T \end{bmatrix}^T \\
T = k_T(V_w, \alpha)\Omega^2
\end{cases} \tag{5}$$

where Ω denotes the fan rotation speed. $k_T(V_w, \alpha)$ is the thrust coefficient.

When the fan is operating, remote airflow of speed V_c is ingested into the fan and accelerated to V_e when exhausted from the fan. This exhaust velocity V_e can be derived from the momentum theory of the duct-fan system:

$$V_e = V_c + V_i = -\frac{w - D_z}{2} + \sqrt{\left(\frac{w - D_z}{2}\right)^2 + \frac{T}{2\rho A}} \tag{6}$$

where V_i denotes the induced velocity of the local flow at the fan. The area of the fan disc is denoted as A.

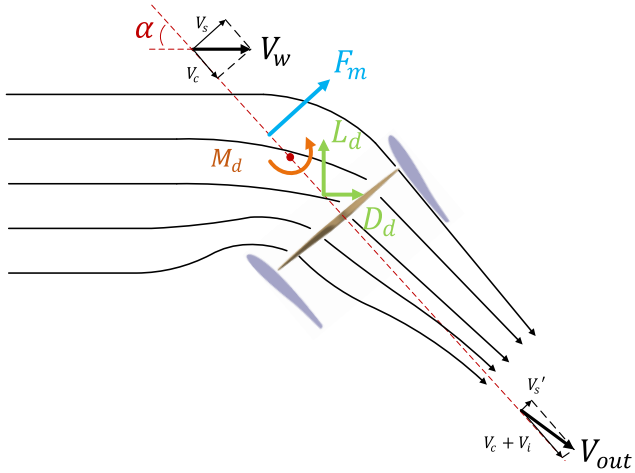

FIGURE 4. Illustration of aerodynamic effects on the duct.

Moment $\mathbf{M}_{cs}$ created by the control surfaces is regarded as the driving moment of the aircraft. Its expression is given by:

$$\mathbf{M}_{cs} = k_{cs} V_e^2 \mathbf{H}\mathbf{c} \quad \begin{cases} \mathbf{H} = \begin{bmatrix} -l_1 & 0 & l_1 & 0 \\ 0 & -l_1 & 0 & l_1 \\ l_2 & l_2 & l_2 & l_2 \end{bmatrix} \\ \mathbf{c} = \begin{bmatrix} c_1 & c_2 & c_3 & c_4 \end{bmatrix}^T \end{cases} \tag{7}$$

where c_i denotes the deflection angle of the i-th control surface. k_{cs} is a constant coefficient. l_1 is the lever arm with respect to roll/pitch axis and l_2 is the lever arm with respect to yaw axis.

2) DUCT EFFECTS

Momentum drag $\mathbf{F}_m$, duct body force $\mathbf{F}_d$ and duct aerodynamic pitching moment $\mathbf{M}_d$ are important factors that differ the ducted fan from a single exposed rotor (e.g. a helicopter) or a pure solid shape (e.g. a wing) [32]. They are presented on 2-D plane in Fig.4.

Momentum drag is a reaction to momentum increment of the air component orthogonal to the fan axis [33]. Additionally, with relative motion to a fluid, the duct shape is subject to a body force which is proportional to the square of the airspeed.

$$\begin{aligned} \mathbf{F}_m &= -\gamma_m \rho \mathrm{A} V_e \begin{bmatrix} u - D_x & v - D_y & 0 \end{bmatrix}^T \\ \mathbf{F}_d &= \begin{bmatrix} -(k_{Ld}(\Omega,\alpha)\cos\alpha + k_{Dd}(\Omega,\alpha)\sin\alpha)\cos\beta \\ -(k_{Ld}(\Omega,\alpha)\cos\alpha + k_{Dd}(\Omega,\alpha)\sin\alpha)\sin\beta \\ -k_{Ld}(\Omega,\alpha)\sin\alpha + k_{Dd}(\Omega,\alpha)\cos\alpha \end{bmatrix} V_w^2 \\ \gamma_m &= \left(V_s - V_s'\right)/V_s \end{aligned} \tag{8}$$

where coefficient γ_m is introduced as damping rate. V_w is the airspeed defined by (2). $k_{Ld}(\Omega,\alpha)$ and $k_{Dd}(\Omega,\alpha)$ are duct lift and duct drag coefficients.

Duct aerodynamic pitching moment $\mathbf{M}_d$ is a result from asymmetric pressure distribution on the duct body [33], mainly on the duct lip. Basically, this moment can be expressed as [3]:

$$\mathbf{M}_d = \boldsymbol{\varepsilon}_m sk(\mathbf{F}_m) + \boldsymbol{\varepsilon}_d sk(\mathbf{F}_d) \tag{9}$$

where $\boldsymbol{\varepsilon}_m$ and $\boldsymbol{\varepsilon}_d$ denote the lever arms of momentum drag and duct body force, respectively.

The mathematic expression of this moment consists of both proportional and quadratic terms with respect to airspeed V_w, the coefficients of which are complicatedly coupled with AOA α and fan rotation speed Ω [34]. To demonstrate the complexity of this moment, CFD results for the ducted fan studied in this paper are shown in Fig.6, in which positive moment and negative moment correspond respectively with nose up and nose down of the aircraft.

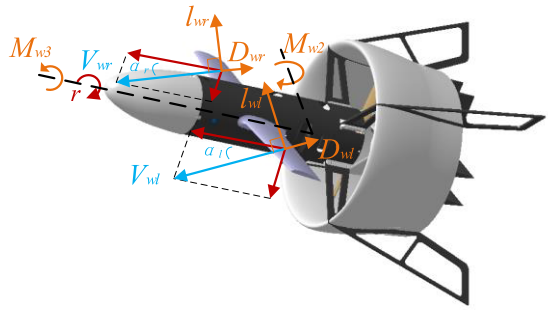

FIGURE 5. Illustration of definitions and aerodynamic effects on the wing.

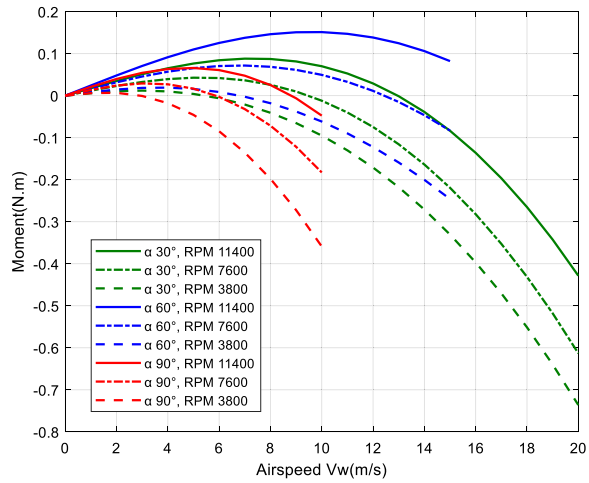

FIGURE 6. CFD results of duct aerodynamic pitching moment under different airspeed, angle of attack and fan rotation speed.

3) FRONT WING EFFECTS

Aerodynamic effects on the front wing consist of wing force $\mathbf{F}_w$ and wing moment $\mathbf{M}_w$. First, we defined the local airspeeds and local AOAs in associated with the left wing and the right wing (See Fig.5).

$$\begin{aligned} V_{wl} &= \sqrt{(u + rl_w - D_x)^2 + (w - D_z)^2} \\ V_{wr} &= \sqrt{(u - rl_w - D_x)^2 + (w - D_z)^2} \end{aligned}$$

$$\begin{aligned}\cos\alpha_l &= -\left(w - D_z\right)/V_{wl}, 0 \le \alpha_l \le \pi \\ \cos\alpha_r &= -\left(w - D_z\right)/V_{wr}, 0 \le \alpha_r \le \pi\end{aligned} \tag{10}$$

where l_w is the lever arm from the aerodynamic center of the left/right wing part to the Z_b axis.

Wing force $\mathbf{F}_w$ is the resultant force of the lifts and drags:

$$\begin{aligned}\mathbf{F}_w &= \begin{bmatrix} -\left(L_{wl}\cos\alpha_l + L_{wr}\cos\alpha_r + D_{wl}\sin\alpha_l + D_{wr}\sin\alpha_r\right) \\ 0 \\ -L_{wl}\sin\alpha_l - L_{wr}\sin\alpha_r + D_{wl}\cos\alpha_l + D_{wr}\cos\alpha_r \end{bmatrix} \\ L_{wl} &= k_{Lw}(\alpha_l)V_{wl}^2, L_{wr} = k_{Lw}(\alpha_r)V_{wr}^2 \\ D_{wl} &= k_{Dw}(\alpha_l)V_{wl}^2, D_{wr} = k_{Dw}(\alpha_r)V_{wr}^2\end{aligned} \tag{11}$$

where $k_{Lw}(\alpha)$ and $k_{Dw}(\alpha)$ are lift and drag coefficients of the half wing part which are functions of AOA.

Wing moment $\mathbf{M}_w$ is given as:

$$\mathbf{M}_w = \begin{bmatrix} 0 \\ M_{w2} \\ M_{w3} \end{bmatrix} = \begin{bmatrix} 0 \\ k_{Mw}(\alpha_l)V_{wl}^2 + k_{Mw}(\alpha_r)V_{wr}^2 \\ -l_w L_{wl} + l_w L_{wr} \end{bmatrix} \tag{12}$$

where $k_{Mw}(\alpha)$ is moment coefficient of the half wing part which is a function of AOA.

4) OTHER TERMS

As for the rest terms of (3), fan torque $\mathbf{M}_{fan}$, anti-rotation torque $\mathbf{M}_f$ generated by the fixed flaps, and fan gyroscopic effect $\mathbf{M}_g$ are given as:

$$\begin{aligned}\mathbf{M}_{fan} &= \begin{bmatrix} 0 & 0 & k_Q(V_w, \alpha)\Omega^2 \end{bmatrix}^T \\ \mathbf{M}_f &= \begin{bmatrix} 0 & 0 & k_f V_e^2 \end{bmatrix}^T \\ \mathbf{M}_g &= \begin{bmatrix} -q & p & 0 \end{bmatrix}^T J_{fan}\Omega\end{aligned} \tag{13}$$

where $k_Q(V_w, \alpha)$ is the torque coefficient. k_f is a constant coefficient and J_{fan} denotes the inertia of the fan.

III. NOMINAL NEURAL NETWORKS DESIGN

In this section, a novel neural networks control strategy for nonlinear system is proposed. First, we divide the system dynamics into two parts. One is completely known and formulated into a reference system containing the reference inputs and the desired dynamics. The other part consists of all the uncertainties. Then neural networks are introduced to reconstruct the unknown system dynamics. In terms of NNs learning algorithm, projection operators and state predictors are invoked. To track the reference system, adaptive control law with a dynamic form is designed to cancel the tracking errors.

Consider the following nonlinear system:

$$\dot{\mathbf{x}} = \mathbf{f}(\mathbf{x}) + \mathbf{g}(\mathbf{x})\mathbf{u} \tag{14}$$

where $\mathbf{x} = \mathbf{x}(t) \in \mathbb{R}^n$, $\mathbf{u} = \mathbf{u}(t) \in \mathbb{R}^m$ (with $n \ge m$), respectively denote the state vector, and the control input vector; Functions $\mathbf{f} : \mathbb{R}^n \to \mathbb{R}^n$, $\mathbf{g} : \mathbb{R}^n \to \mathbb{R}^{n\times m}$, are continuously differentiable. Taking consideration of unknown system dynamics and parameter uncertainties, we divide system (14) into the following two parts:

$$\begin{cases} \mathbf{f}(\mathbf{x}) = \bar{\mathbf{f}}(\mathbf{x}) + \tilde{\mathbf{f}}(\mathbf{x}) \\ \mathbf{g}(\mathbf{x}) = \bar{\mathbf{g}}(\mathbf{x}) + \tilde{\mathbf{g}}(\mathbf{x}) \\ \mathbf{u} = \bar{\mathbf{u}} + \tilde{\mathbf{u}} \end{cases} \tag{15}$$

where $\bar{\mathbf{f}}(\mathbf{x})$ and $\bar{\mathbf{g}}(\mathbf{x})$ are completely known or measurable while $\tilde{\mathbf{f}}(\mathbf{x})$ and $\tilde{\mathbf{g}}(\mathbf{x})$ contain all the uncertainties and measurement errors. Correspondingly, the control input is divided into a nominal term $\bar{\mathbf{u}}$ and an adaptive term $\tilde{\mathbf{u}}$. Then, we can determine the desired dynamic performance $\dot{\mathbf{x}}_m$ and nominal input $\bar{\mathbf{u}}$ to form a reference system such that:

$$\dot{\mathbf{x}}_m = \bar{\mathbf{f}}(\mathbf{x}) + \bar{\mathbf{g}}(\mathbf{x})\bar{\mathbf{u}} \tag{16}$$

With the definitions (15)(16), we can rewrite the nonlinear system (14) into:

$$\begin{aligned}\dot{\mathbf{x}} &= \dot{\mathbf{x}}_m + \mathbf{e} \\ \mathbf{e} &= \tilde{\mathbf{f}}(\mathbf{x}) + \bar{\mathbf{g}}(\mathbf{x})\tilde{\mathbf{u}} + \tilde{\mathbf{g}}(\mathbf{x})\tilde{\mathbf{u}} + \tilde{\mathbf{g}}(\mathbf{x})\bar{\mathbf{u}}\end{aligned} \tag{17}$$

In prior, we introduce an auxiliary system to handle the system uncertainties. First, we reconstruct the uncertain terms $\tilde{\mathbf{f}}(\mathbf{x})$, $\tilde{\mathbf{g}}(\mathbf{x})$ with parameterized neural networks:

$$\begin{cases} \tilde{\mathbf{f}}(\mathbf{x}) = \mathbf{W}_{\mathbf{f}}^T \mathbf{\Phi}_{\mathbf{f}}(\mathbf{x}) \\ \tilde{\mathbf{g}}(\mathbf{x}) = \mathbf{W}_{\mathbf{g}}^T \mathbf{\Phi}_{\mathbf{g}}(\mathbf{x}) \end{cases} \tag{18}$$

where $\mathbf{W}_{\mathbf{f}} \in \mathbb{R}^{N_f\times n}$ and $\mathbf{W}_{\mathbf{g}} \in \mathbb{R}^{N_g\times n}$ denote the unknown weight matrices. $\mathbf{\Phi}_{\mathbf{f}} : \mathbb{R}^n \to \mathbb{R}^{N_f}$, $\mathbf{\Phi}_{\mathbf{g}} : \mathbb{R}^n \to \mathbb{R}^{N_g\times m}$ denote the proper basis functions with N_f, N_g denoting the numbers of neurons. Subsequently, the nonlinear system (14) can be reformed into the following:

$$\dot{\mathbf{x}} = \left[\bar{\mathbf{f}}(\mathbf{x}) + \mathbf{W}_{\mathbf{f}}^T \mathbf{\Phi}_{\mathbf{f}}(\mathbf{x})\right] + \left[\bar{\mathbf{g}}(\mathbf{x}) + \mathbf{W}_{\mathbf{g}}^T \mathbf{\Phi}_{\mathbf{g}}(\mathbf{x})\right]\left(\bar{\mathbf{u}} + \tilde{\mathbf{u}}\right) \tag{19}$$

With this parameterization, the system uncertainty corresponds to the uncertainty of weight matrices. Based on the parameterized system, we design a state predictor to estimate the dynamics of the original nonlinear system:

$$\dot{\hat{\mathbf{x}}} = \bar{\mathbf{f}}(\mathbf{x}) + \hat{\mathbf{W}}_{\mathbf{f}}^T \mathbf{\Phi}_{\mathbf{f}}(\mathbf{x}) + \bar{\mathbf{g}}(\mathbf{x})\mathbf{u} + \hat{\mathbf{W}}_{\mathbf{g}}^T \mathbf{\Phi}_{\mathbf{g}}(\mathbf{x})\mathbf{u} - \mathbf{K}_{\mathbf{x}}\left(\hat{\mathbf{x}} - \mathbf{x}\right) \tag{20}$$

where $\mathbf{K}_{\mathbf{x}} = \mathrm{diag}(K_{\mathbf{x}1}, \cdots, K_{\mathbf{x}n})$ is a positive definite gain matrix and $\hat{\mathbf{W}}_{\mathbf{f}}$, $\hat{\mathbf{W}}_{\mathbf{g}}$ are the estimations of $\mathbf{W}_{\mathbf{f}}$, $\mathbf{W}_{\mathbf{g}}$. The objective is that the predictor (20) tracks the nonlinear system dynamics (19). To achieve this, the following evolutions are designed:

$$\begin{aligned}\dot{\hat{\mathbf{W}}}_{\mathbf{f}} &= \mathbf{\Gamma}_{\mathbf{f}}\mathbf{Proj}_{\Omega_{\mathbf{f}}}(\hat{\mathbf{W}}_{\mathbf{f}}, -\mathbf{\Phi}_{\mathbf{f}}(\mathbf{x})\left(\hat{\mathbf{x}} - \mathbf{x}\right)^T) \\ \dot{\hat{\mathbf{W}}}_{\mathbf{g}} &= \mathbf{\Gamma}_{\mathbf{g}}\mathbf{Proj}_{\Omega_{\mathbf{g}}}(\hat{\mathbf{W}}_{\mathbf{g}}, -\mathbf{\Phi}_{\mathbf{g}}(\mathbf{x})\mathbf{u}\left(\hat{\mathbf{x}} - \mathbf{x}\right)^T)\end{aligned} \tag{21}$$

where $\mathbf{\Gamma}_{\mathbf{f}} = \mathrm{diag}(\Gamma_{\mathbf{f}1}, \cdots, \Gamma_{\mathbf{f}n})$ and $\mathbf{\Gamma}_{\mathbf{g}} = \mathrm{diag}(\Gamma_{\mathbf{g}1}, \cdots, \Gamma_{\mathbf{g}n})$ are constant learning rate matrices which are positive definite. $\mathbf{Proj}_{\Omega}$ denotes the projection operator of matrix. $\Omega_{\mathbf{f}} \subset \mathbb{R}^{n\times N_f}$, $\Omega_{\mathbf{g}} \subset \mathbb{R}^{n\times N_g}$ are convex compact sets that $\hat{\mathbf{W}}_{\mathbf{f}} \in \Omega_{\mathbf{f}}$, $\hat{\mathbf{W}}_{\mathbf{g}} \in \Omega_{\mathbf{g}}$. See Appendix A for detailed definitions and

properties of projection operator. Combining (20) with (21), an auxiliary system is established as [35]:

$$\begin{cases} \dot{\hat{\mathbf{x}}} = \bar{\mathbf{f}}(\mathbf{x}) + \hat{\mathbf{W}}_{\mathbf{f}}^T \mathbf{\Phi}_{\mathbf{f}} + \bar{\mathbf{g}}(\mathbf{x})\mathbf{u} + \hat{\mathbf{W}}_{\mathbf{g}}^T \mathbf{\Phi}_{\mathbf{g}}\mathbf{u} - \mathbf{K}_{\mathbf{x}}\left(\hat{\mathbf{x}} - \mathbf{x}\right) \\ \dot{\hat{\mathbf{W}}}_{\mathbf{f}} = \mathbf{\Gamma}_{\mathbf{f}}\mathbf{Proj}_{\Omega_{\mathbf{f}}}(\hat{\mathbf{W}}_{\mathbf{f}}, -\mathbf{\Phi}_{\mathbf{f}}\left(\hat{\mathbf{x}} - \mathbf{x}\right)^T) \\ \dot{\hat{\mathbf{W}}}_{\mathbf{g}} = \mathbf{\Gamma}_{\mathbf{g}}\mathbf{Proj}_{\Omega_{\mathbf{g}}}(\hat{\mathbf{W}}_{\mathbf{g}}, -\mathbf{\Phi}_{\mathbf{g}}\mathbf{u}\left(\hat{\mathbf{x}} - \mathbf{x}\right)^T) \end{cases} \tag{22}$$

Recalling (17), In order to track the reference system $\dot{\mathbf{x}}_m$, specific adaptive input $\tilde{\mathbf{u}}$ is to be adopted such that $\mathbf{e} = 0$. On the first attempt, we can simply choose the adaptive term as $\tilde{\mathbf{u}} = -[\bar{\mathbf{g}}(\mathbf{x}) + \tilde{\mathbf{g}}(\mathbf{x})]^{\dagger}[\tilde{\mathbf{f}}(\mathbf{x}) + \tilde{\mathbf{g}}(\mathbf{x})\bar{\mathbf{u}}]$ with '$(.)^{\dagger}$' denoting the pseudo-inverse of non-square matrix. However, this control law is not expressed in affine and the inverse calculation could make $\tilde{\mathbf{u}}$ too sensitive to the noise in $\tilde{\mathbf{g}}(\mathbf{x})$ in some special cases, and probably results in unacceptable oscillation or divergence of the closed-loop system. Instead, we design the adaptive control input $\tilde{\mathbf{u}}$ by a dynamic form as:

$$\begin{aligned} \dot{\tilde{\mathbf{u}}} &= -\mathbf{\Gamma}_{\mathbf{u}}\left[\bar{\mathbf{g}}(\mathbf{x}) + \hat{\mathbf{W}}_{\mathbf{g}}^T \mathbf{\Phi}_{\mathbf{g}}\right]^T \hat{\mathbf{e}}(\tilde{\mathbf{u}}) \\ \hat{\mathbf{e}}(\tilde{\mathbf{u}}) &= \hat{\mathbf{W}}_{\mathbf{f}}^T \mathbf{\Phi}_{\mathbf{f}} + \bar{\mathbf{g}}(\mathbf{x})\tilde{\mathbf{u}} + \hat{\mathbf{W}}_{\mathbf{g}}^T \mathbf{\Phi}_{\mathbf{g}}\tilde{\mathbf{u}} + \hat{\mathbf{W}}_{\mathbf{g}}^T \mathbf{\Phi}_{\mathbf{g}}\bar{\mathbf{u}} \end{aligned} \tag{23}$$

where $\mathbf{\Gamma}_{\mathbf{u}} = \mathrm{diag}(\Gamma_{\mathbf{u}1}, \cdots, \Gamma_{\mathbf{u}n})$, $\Gamma_{\mathbf{u}i} > 0$ is a constant gain matrix.

Theorem 1: The states and dynamics of auxiliary system (22) converge to those of original nonlinear system. And the state prediction error $\tilde{\mathbf{x}} = \hat{\mathbf{x}} - \mathbf{x}$ is upper bounded by:

$$\left\|\tilde{\mathbf{x}}\right\|^2 \leq \lambda_{\max}(\mathbf{\Gamma}_{\mathbf{f}}^{-1})\mathbf{W}_{\mathbf{f}\max} + \lambda_{\max}(\mathbf{\Gamma}_{\mathbf{g}}^{-1})\mathbf{W}_{\mathbf{g}\max} \tag{24}$$

Proof: The proof of *Theorem 1* is given in Appendix B.

Theorem 2: The dynamics of the closed-loop system with auxiliary system (22) and control input (23) tracks the desired dynamic performance $\dot{\mathbf{x}}_m$ with tracking error $\mathbf{e} \to 0$.

Proof: The proof of *Theorem 2* is given in Appendix C.

Remark 2: Known parts $\bar{\mathbf{f}}(\mathbf{x})$ and $\bar{\mathbf{g}}(\mathbf{x})$ can be arbitrarily chosen, usually constant to make $\dot{\mathbf{x}}_m$ linear. Even if we remain them as nonlinear functions, there exists a certain input $\bar{\mathbf{u}}$ such that $\dot{\mathbf{x}}_m$ can be linearized through feedback linearization technique. It is worth pointing out that more information about these two parts helps achieve more satisfactory control performance.

Due to the introduction of projection operator, it is guaranteed that the tracking errors of both state predictor and NNs weights are upper bounded during the NN learning procedure. According to *Theorem 1*, the upper bound of the state prediction error (24) is exclusive of time. This implies a stronger property than UUB that the transient performance of these tracking errors maintains upper bounded especially at the early stage of parameter adaption. Consequently, in order to achieve fast convergence of the tracking process, it is reliable to increase the learning rates $\mathbf{\Gamma}_{\mathbf{f}}$, $\mathbf{\Gamma}_{\mathbf{g}}$ without the occurrence of parameter overshoot. In other perspective, large values of learning rates result in high-gain feedback control, which, in some case, could cause serious oscillations of the system states and reduce tolerance of time delay. This limits the high-frequency disturbance rejection ability of the closed-loop system. On the contrary, the designed adaptive control input (23) shares the same structure as a low-pass filter that prevents the actuators from vibrating with high-frequency. As a result, the deterioration in robustness resulting from large learning rates is neutralized. This also leads to the attenuation of noises from both states and input signals. In conclusion, the closed-loop system with the auxiliary system (22) and adaptive control input (23) is capable of fast parameter convergence with good disturbance rejection performance, and works well under certain noises. In Section V, simulation results are shown in Fig.8, Fig.9 and Fig.10 to demonstrate this property.

IV. FLIGHT CONTROL DESIGN

In this section, aircraft dynamics (4) is reconstructed into a better arranged nonlinear cascade form. Then, we apply the proposed NNs-based control scheme on two cascade closed-loop systems. With all the efforts, the aircraft is able to track a certain trajectory from hover to high-speed flight.

A. SYSTEM RECONSTRUCTION

Define the state variables and the regulated system inputs:

$$\begin{aligned} \mathbf{x} &= \begin{bmatrix} \mathbf{x}_1^T & \mathbf{x}_2^T & \mathbf{x}_3^T & \mathbf{x}_4^T \end{bmatrix}^T = \begin{bmatrix} \mathbf{p}^T & \mathbf{V}_E^T & \boldsymbol{\xi}^T & \boldsymbol{\omega}^T \end{bmatrix}^T \\ \mathbf{u} &= [T \quad \mathbf{u}_a^T]^T \end{aligned} \tag{25}$$

whereas $\mathbf{x}_i = [x_{i1} \ x_{i2} \ x_{i3}]^T \in \mathbb{R}^3, i = 1, \cdots, 4$. $T \in \mathbb{R}$ marks the thrust input and $\mathbf{u}_a \in \mathbb{R}^3$ marks the regulated moment inputs. The regulated moment inputs are obtained by:

$$\mathbf{u}_a = \begin{bmatrix} u_{a1} & u_{a2} & u_{a3} \end{bmatrix}^T = \mathbf{Hc} \tag{26}$$

where mapping matrix $\mathbf{H}$ and deflection angles of control surfaces $\mathbf{c}$ are given in (7). Since there are no derivative terms in expression (7), we can conclude that virtual control input $\mathbf{u}_a$ shares the same response dynamics with practical movements of the actuators. Subsequently, we separate the input terms apart from the dynamic system (4) and integrate the rest into standard nonlinear forms, let:

$$\begin{aligned} \mathbf{f}_1(\mathbf{x}) &= \frac{1}{m}[\mathbf{F}_m + \mathbf{F}_d + \mathbf{F}_w] \\ \mathbf{g}_1(\mathbf{x}_3) &= \mathbf{R} \\ \mathbf{f}_2(\mathbf{x}) &= \mathbf{J}^{-1}\left[\mathbf{M}_{fan} + \mathbf{M}_f + \mathbf{M}_g + \mathbf{M}_d + \mathbf{M}_w + \mathbf{J}\omega sk(\boldsymbol{\omega})\right] \\ \mathbf{g}_2(\mathbf{x}, T) &= k_{cs}V_e^2\mathbf{J}^{-1} \end{aligned} \tag{27}$$

Eventually, we complete the system descriptions by substituting (25)(26)(27) into (4):

$$\begin{cases} \dot{\mathbf{x}}_1 = \mathbf{x}_2 \\ \dot{\mathbf{x}}_2 = \mathbf{g}_1(\mathbf{x}_3)\mathbf{f}_1 + \begin{bmatrix} 0 & 0 & g \end{bmatrix}^T - \mathbf{g}_1(\mathbf{x}_3)\begin{bmatrix} 0 & 0 & T/m \end{bmatrix}^T \\ \dot{\mathbf{x}}_3 = \mathbf{Q}\mathbf{x}_4 \\ \dot{\mathbf{x}}_4 = \mathbf{f}_2 + \mathbf{g}_2(\mathbf{x}, T)\mathbf{u}_a \end{cases} \tag{28}$$

B. FLIGHT CONTROL DESIGN

Essentially, the hover to high-speed transition is a process that the aircraft continuously pitches down and accelerates to a

high cruising speed. To this end, the objective of controller design is to force the aircraft tracking a certain trajectory that formulates this process.

The first 2 rows of (28) are position and velocity dynamics of the aircraft, which is generally considered as system outer-loop. Meanwhile, the last 2 rows of (28) demonstrate the attitude dynamics of the rigid body, which is generally regarded as system inner-loop. Together, these two loops establish an underactuated cascade structure of the aircraft system. Furthermore, although equations (28) can describe the whole transition process without constructively change, component values of the system vary greatly from the original hover condition to the final high-speed flight condition as aforementioned. In terms of control strategy, we apply the nominal neural networks design in Section III on both inner-loop and outer-loop.

1) INNER-LOOP DESIGN

The attitude dynamics is extracted from the last 2 rows of system (28):

$$\begin{cases} \dot{\mathbf{x}}_3 = \mathbf{Q}\mathbf{x}_4 \\ \dot{\mathbf{x}}_4 = \mathbf{f}_2 + \mathbf{g}_2(\mathbf{x}, T)\mathbf{u}_a \end{cases} \tag{29}$$

Note that the input signals are coupled with both thrust input T and moment inputs $\mathbf{u}_a$. In this paper, we only consider $\mathbf{u}_a$ to be the control inputs of the inner-loop while a relevant neural network is to be designed to estimate and compensate for the effect of T. Meanwhile, Since $\mathbf{Q}$ is measurable and consist of no uncertainty, we only introduce neural networks to reconstruct the dynamics of angular velocity $\mathbf{x}_4$:

$$\dot{\mathbf{x}}_4 = \left[\bar{\mathbf{f}}_2 + \mathbf{W}_1^T \mathbf{\Phi}_1\right] + \left[\bar{\mathbf{g}}_2 + \mathbf{W}_2^T \mathbf{\Phi}_2\right]\left(\bar{\mathbf{u}}_a + \tilde{\mathbf{u}}_a\right) \tag{30}$$

In practice, neither $\mathbf{f}_2$, the aerodynamic moment, nor $\mathbf{g}_2$, the efficiency of control surfaces is measurable. In this case, let: $\bar{\mathbf{f}}_2 = 0, \bar{\mathbf{g}}_2 = \mathbf{g}_{2h} = \text{const}$ whereas $\mathbf{g}_{2h}$ is the value of $\mathbf{g}_2(\mathbf{x}, T)$ at hover working point which can be easily determined by experiments. Then, the reference system of $\mathbf{x}_4$ is designed as linear feedback system:

$$\begin{aligned} \dot{\mathbf{x}}_{4m} &= \mathbf{g}_{2h}\bar{\mathbf{u}}_a \\ \bar{\mathbf{u}}_a &= \mathbf{K}_4\left(\mathbf{x}_{4d} - \mathbf{x}_4\right) \end{aligned} \tag{31}$$

where $\mathbf{K}_4$ is a positive feedback gain matrix, and $\mathbf{x}_{4d}$ is the reference input of $\mathbf{x}_4$. Hence, the nonlinear dynamics of angular velocity $\mathbf{x}_4$ can be rewritten into:

$$\begin{aligned} \dot{\mathbf{x}}_4 &= \dot{\mathbf{x}}_{4m} + \mathbf{e}_4 \\ \mathbf{e}_4 &= \mathbf{W}_1^T \mathbf{\Phi}_1 + \mathbf{g}_{2h}\tilde{\mathbf{u}}_a + \mathbf{W}_2^T \mathbf{\Phi}_2 \tilde{\mathbf{u}}_a + \mathbf{W}_2^T \mathbf{\Phi}_2 \bar{\mathbf{u}}_a \end{aligned} \tag{32}$$

Subsequently, the auxiliary system is designed as:

$$\begin{cases} \dot{\hat{\mathbf{x}}}_4 = \dot{\mathbf{x}}_{4m} + \hat{\mathbf{e}}_4 - \mathbf{K}_{\mathbf{x}1}\left(\hat{\mathbf{x}}_4 - \mathbf{x}_4\right) \\ \hat{\mathbf{e}}_4 = \hat{\mathbf{W}}_1^T \mathbf{\Phi}_1 + \mathbf{g}_{2h}\tilde{\mathbf{u}}_a + \hat{\mathbf{W}}_2^T \mathbf{\Phi}_2 \tilde{\mathbf{u}}_a + \hat{\mathbf{W}}_2^T \mathbf{\Phi}_2 \bar{\mathbf{u}}_a \\ \dot{\hat{\mathbf{W}}}_1 = \mathbf{\Gamma}_1 \mathbf{Proj}_{\Omega_1}(\hat{\mathbf{W}}_1, -\mathbf{\Phi}_1\left(\hat{\mathbf{x}}_4 - \mathbf{x}_4\right)^T) \\ \dot{\hat{\mathbf{W}}}_2 = \mathbf{\Gamma}_2 \mathbf{Proj}_{\Omega_2}(\hat{\mathbf{W}}_2, -\mathbf{\Phi}_2 \mathbf{u}_a\left(\hat{\mathbf{x}}_4 - \mathbf{x}_4\right)^T) \end{cases} \tag{33}$$

Note that $\mathbf{g}_2$ represents the efficiency of the control surfaces which is positive definite. Thus, the application of (23) on adaptive control input $\tilde{\mathbf{u}}_a$ can be simplified as:

$$\dot{\tilde{\mathbf{u}}}_a = -\mathbf{\Gamma}_{\mathbf{u}a}\hat{\mathbf{e}}_4 \tag{34}$$

Eventually, we complete the inner-loop into PD controller by defining the reference system of $\mathbf{x}_3$:

$$\begin{aligned} \mathbf{x}_{4d} &= \mathbf{Q}^{-1}\left\{\mathbf{K}_3\left(\mathbf{x}_{3d} - \mathbf{x}_3\right) - \left(\mathbf{g}_{2h}\mathbf{K}_4\right)^{-1} \right. \\ &\quad \left. \cdot \left(\frac{\mathrm{d}\mathbf{Q}}{\mathrm{d}\mathbf{x}_3}\right)^T \Lambda\left(\mathbf{Q}\mathbf{x}_4\right)\mathbf{x}_4\right\} \\ \ddot{\mathbf{x}}_{3m} &= -\mathbf{g}_{2h}\mathbf{K}_4\mathbf{K}_3\mathbf{x}_3 - \mathbf{g}_{2h}\mathbf{K}_4\dot{\mathbf{x}}_3 + \mathbf{g}_{2h}\mathbf{K}_4\mathbf{K}_3\mathbf{x}_{3d} \\ \left(\frac{\mathrm{d}\mathbf{Q}}{\mathrm{d}\mathbf{x}_3}\right)^T &= \left[\left(\frac{\mathrm{d}\mathbf{Q}}{\mathrm{d}x_{31}}\right)^T \quad \left(\frac{\mathrm{d}\mathbf{Q}}{\mathrm{d}x_{32}}\right)^T \quad \left(\frac{\mathrm{d}\mathbf{Q}}{\mathrm{d}x_{33}}\right)^T\right]_{3\times 9} \end{aligned} \tag{35}$$

where $\mathbf{K}_3$ is a positive feedback gain matrix. The notation 'Λ (.)' denotes a special operator for a vector $\mathbf{x} \in \mathbb{R}^3$ that:

$$\Lambda\left(\mathbf{x}\right) = \left[x_1 \cdot I_{3\times 3} \quad x_2 \cdot I_{3\times 3} \quad x_3 \cdot I_{3\times 3}\right]^T \tag{36}$$

Theorem 3: To the closed-loop system for (29) with control strategy of (31)(33)(34)(35), the state $\mathbf{x}_3$ (Euler angles) tracks the reference input $\mathbf{x}_{3d}$ with desired dynamics $\ddot{\mathbf{x}}_{3m}$ and tracking error goes to zero with time.

Proof: The proof of *Theorem 3* is given in Appendix D.

2) OUTER-LOOP DESIGN

By the accomplishment of the inner-loop, the Euler angle $\mathbf{x}_3$ always tracks the reference input $\mathbf{x}_{3d}$ with bounded tracking error $\tilde{\mathbf{x}}_3$ which converges to zero. In terms of outer-loop design, we consider $\mathbf{x}_3, T$ as the inputs to the translation dynamics, and $\mathbf{x}_{3d}, u_1$ as the inputs to the dynamic system of $\mathbf{x}_3, T$. The tracking errors between $\mathbf{x}_{3d}, u_1$ and $\mathbf{x}_3, T$ are respectively denoted as $\tilde{\mathbf{x}}_3, \tilde{T}$, which are considered as input uncertainties of the translational dynamics.

$$\begin{cases} \mathbf{x}_3 = \mathbf{u}_3 + \tilde{\mathbf{x}}_3, & \mathbf{u}_3\mathbf{x}_{3d} \\ T = mu_1 + \tilde{T}, & u_1 = k_{T0}\Omega^2/m \end{cases} \tag{37}$$

where k_{T0} is a constant thrust coefficient that could be arbitrarily chosen. In this paper, k_{T0} is determined as the value of k_T at hover condition which is easily acquired by experiments. Subsequently, the translation dynamics is extracted from the first 2 rows of system (28):

$$\begin{cases} \dot{\mathbf{x}}_1 = \mathbf{x}_2 \\ \dot{\mathbf{x}}_2 = \mathbf{g}_1(\mathbf{x}_3)\mathbf{f}_1 + \begin{bmatrix} 0 & 0 & g \end{bmatrix}^T - \mathbf{g}_1(\mathbf{x}_3)\begin{bmatrix} 0 & 0 & T/m \end{bmatrix}^T \end{cases} \tag{38}$$

Note that the gravity-excluded resultant force acting on the aircraft can be completely measured and calculated by an IMU sensor in practice. Based on this, different from the inner-loop design, the main issue for outer-loop design is to compensate for the input uncertainties defined by (37). Let:

$$\begin{cases} \mathbf{u}_3 = \bar{\mathbf{u}}_3 + \tilde{\mathbf{u}}_3 \\ u_1 = \bar{u}_1 + \tilde{u}_1 \\ \Upsilon = \mathbf{f}_1 - \begin{bmatrix} 0 & 0 & \bar{u}_1 + \tilde{u}_1 + \tilde{T}/m \end{bmatrix}^T \end{cases} \tag{39}$$

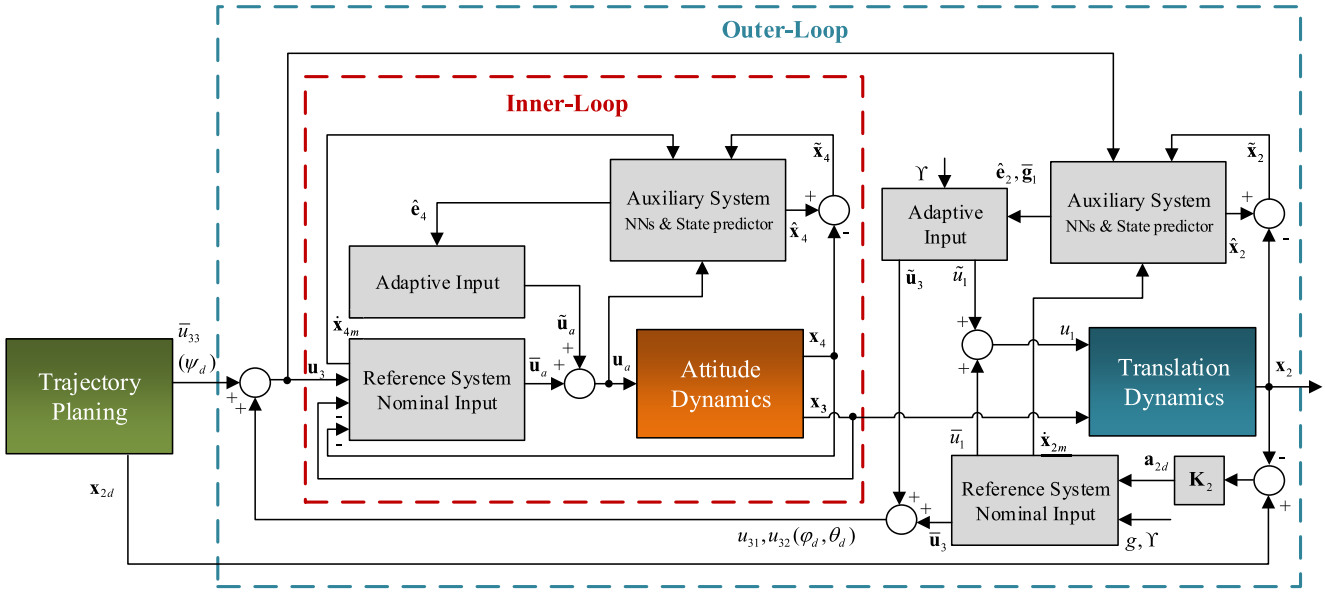

FIGURE 7. Neural-networks-based flight control structure.

where $\Upsilon = [\Upsilon_1 \;\; \Upsilon_2 \;\; \Upsilon_3]^T$ denotes the acceleration due to the gravity-excluded resultant force which are completely measurable. In terms of the rotation matrix $\mathbf{g}_1(\mathbf{x}_3)$, we divide it into pure $\mathbf{u}_3$-related terms and uncertainty containing terms by using the first-order Taylor expansion. First, notice that there always exists a NN that:

$$\mathbf{g}_1 \triangleq (\mathbf{x}_3) = \bar{\mathbf{g}}_1 + \tilde{\mathbf{g}}_1 \Lambda\left(\tilde{\mathbf{u}}_3 + \mathbf{W}_3^T \mathbf{\Phi}_3\right)$$
$$\begin{cases} \bar{\mathbf{g}}_1 \triangleq \mathbf{g}_1(\bar{\mathbf{u}}_3) \\ \tilde{\mathbf{g}}_1 \triangleq \left(\dfrac{\partial \mathbf{g}_1(\bar{\mathbf{u}}_3)}{\partial \bar{\mathbf{u}}_3}\right)^T \\ = \left[\left(\frac{\partial \mathbf{g}_1(\bar{\mathbf{u}}_3)}{\partial \bar{u}_{31}}\right)^T \;\; \left(\frac{\partial \mathbf{g}_1(\bar{\mathbf{u}}_3)}{\partial \bar{u}_{32}}\right)^T \;\; \left(\frac{\partial \mathbf{g}_1(\bar{\mathbf{u}}_3)}{\partial \bar{u}_{33}}\right)^T\right]_{3\times 9} \end{cases} \tag{40}$$

where the notation 'Λ (.)' is pre-defined by (36). Then we reconstruct the translation dynamics (38) into:

$$\begin{aligned} \dot{\mathbf{x}}_1 &= \mathbf{x}_2 \\ \dot{\mathbf{x}}_2 &= \left[\bar{\mathbf{g}}_1 + \tilde{\mathbf{g}}_1 \Lambda\left(\tilde{\mathbf{u}}_3 + \mathbf{W}_3^T \mathbf{\Phi}_3\right)\right] \Upsilon + \left[0 \quad 0 \quad g\right]^T \\ &= \bar{\mathbf{g}}_1 \Upsilon_1 + \tilde{\mathbf{g}}_1 \Xi(\Upsilon)\left(\tilde{\mathbf{u}}_3 + \mathbf{W}_3^T \mathbf{\Phi}_3\right) + \left[0 \quad 0 \quad g\right]^T \\ &= \dot{\mathbf{x}}_{2m} + \mathbf{e}_2 \\ \mathbf{e}_2 &= \tilde{\mathbf{g}}_1 \Xi(\Upsilon)\left(\tilde{\mathbf{u}}_3 + \mathbf{W}_3^T \mathbf{\Phi}_3\right) + \bar{\mathbf{g}}_1 \left[0 \;\; 0 \;\; \Upsilon_3 + \bar{u}_1\right]^T \end{aligned} \tag{41}$$

where the reference system with desired dynamics $\dot{\mathbf{x}}_{2m}$ for acceleration $\dot{\mathbf{x}}_2$ is given by:

$$\dot{\mathbf{x}}_{2m} = \bar{\mathbf{g}}_1 \left[\Upsilon_1 \quad \Upsilon_2 \quad -\bar{u}_1\right]^T + \left[0 \quad 0 \quad g\right]^T \tag{42}$$

And the notation 'Ξ' denotes a special operator for a vector $\mathbf{x} \in \mathbb{R}^3$ that:

$$\Xi(\mathbf{x}) = \begin{bmatrix} \mathbf{x} & \mathbf{0}_{3\times 1} & \mathbf{0}_{3\times 1} \\ \mathbf{0}_{3\times 1} & \mathbf{x} & \mathbf{0}_{3\times 1} \\ \mathbf{0}_{3\times 1} & \mathbf{0}_{3\times 1} & \mathbf{x} \end{bmatrix}_{9\times 3} \tag{43}$$

Subsequently, the auxiliary system is designed as:

$$\begin{cases} \dot{\hat{\mathbf{x}}}_2 = \dot{\mathbf{x}}_{2m} + \hat{\mathbf{e}}_2(\tilde{\mathbf{u}}_3, \tilde{u}_1) - \mathbf{K}_{\mathbf{x}2}\left(\hat{\mathbf{x}}_2 - \mathbf{x}_2\right) \\ \hat{\mathbf{e}}_2(\tilde{\mathbf{u}}_3, \tilde{u}_1) = \tilde{\mathbf{g}}_1 \Xi(\Upsilon)\left(\tilde{\mathbf{u}}_3 + \hat{\mathbf{W}}_3^T \mathbf{\Phi}_3\right) \\ \qquad\qquad + \bar{\mathbf{g}}_1 \left[0 \quad 0 \quad \Upsilon_3 + \bar{u}_1\right]^T \\ \dot{\hat{\mathbf{W}}}_3 = \mathbf{\Gamma}_3 \mathbf{Proj}_{\Omega_3}\left[\hat{\mathbf{W}}_3, -\mathbf{\Phi}_3\left(\hat{\mathbf{x}}_2 - \mathbf{x}_2\right)^T \tilde{\mathbf{g}}_1 \Xi(\Upsilon)\right] \end{cases} \tag{44}$$

To complete the outer-loop controller, the nominal control inputs and adaptive control inputs are given as:

$$\begin{cases} \dot{\bar{\mathbf{u}}}_3 = -\mathbf{\Gamma}_{\mathbf{u}3}\left[\tilde{\mathbf{g}}_1 \Xi(\Upsilon)\right]^T \hat{\mathbf{e}}_2(\tilde{\mathbf{u}}_3, \tilde{u}_1) \\ \dot{\bar{u}}_1 = -\Gamma_{u1}\left[0 \;\; 0 \;\; 1\right] \bar{\mathbf{g}}_1^T \hat{\mathbf{e}}_2(\tilde{\mathbf{u}}_3, \tilde{u}_1) \\ \bar{\mathbf{u}}_3 = \left[\bar{u}_{31} \;\; \bar{u}_{32} \;\; \bar{u}_{33}\right]^T = \left[\mu_1 - \chi_1 \;\; \mu_2 - \chi_2 \;\; x_{3d3}\right]^T \\ \bar{u}_1 = \left[0 \;\; 0 \;\; -1\right] \bar{\mathbf{g}}_1^T \left[a_{2dx} \;\; a_{2dy} \;\; a_{2d3} - g\right]^T \end{cases} \tag{45}$$

where

$$\begin{cases} \chi_1 = \arctan\left[\dfrac{a_{2dy}}{(a_{2d3} - g)}\right] \\ \chi_2 = \arctan\left[-\dfrac{a_{2dx}}{(a_{2d3} - g)\cos\bar{u}_{31} + a_{2dy}\sin\bar{u}_{31}}\right] \\ \mu_1 = \arcsin\left[\dfrac{\Upsilon_2}{\sqrt{(a_{2d3} - g)^2 + a_{2dy}^2}}\right] \\ \mu_2 = \arcsin\left[\dfrac{-\Upsilon_1}{\sqrt{\left[(a_{2d3} - g)\cos\bar{u}_{31} + a_{2dy}\sin\bar{u}_{31}\right]^2 + a_{2dx}^2}}\right] \\ a_{2dx} = (a_{2d1}\cos\bar{u}_{33} + a_{2d2}\sin\bar{u}_{33}) \\ a_{2dy} = (-a_{2d1}\sin\bar{u}_{33} + a_{2d2}\cos\bar{u}_{33}) \end{cases} \tag{46}$$

where $\mathbf{a}_{2d} = [a_{2d1}\ a_{2d2}\ a_{2d3}]^T$ is the desired acceleration vector in the inertial frame, which is obtained by a feedback form of velocity $\mathbf{x}_2$ including reference input $\mathbf{x}_{2d}$ and diagonal positive definite gain matrix $\mathbf{K}_2$:

$$\mathbf{a}_{2d} = \mathbf{K}_2(\mathbf{x}_{2d} - \mathbf{x}_2) \tag{47}$$

Since there are no model-linked dynamics on the first row of (38), the controller design ends up with velocity tracking.

Theorem 4: To the closed-loop system for (38) with control strategy of (39)(44)(45)(46)(47), the state $\mathbf{x}_2$ tracks the reference input $\mathbf{x}_{2d}$ with desired dynamics $\dot{\mathbf{x}}_{2m} = \mathbf{a}_{2d}$ and tracking error goes to zero with time.

Proof: The proof of *Theorem 4* is given in Appendix D.

It is also implied in Appendix D that the inputs $\mathbf{x_3}, T$ of the translational dynamics tracks the nominal inputs $\bar{\mathbf{u}}_{\mathbf{3}}, \bar{u}_1$ defined by (45) with all the input uncertainties eliminated.

The complete control structure is shown in Fig.7. Combining the inner-loop and outer-loop designs, the closed-loop system is able to track a certain trajectory which is describe by four independent state variables $[\mathbf{x}_{2d}\ \ x_{3d3}] = [V_{xE}\ \ V_{yE}\ \ V_{zE}\ \ \psi]$ (i.e., velocity in the inertial frame and yaw angle). It is also guaranteed that during the tracking process, the system performance follows a desired reference system. In terms of engineering practice for the aircraft, the reference system is usually determined as linear system formed with PD controllers that the corresponding parameters can be easily tuned at hover. During the hover to high-speed transition process, the system performance always tracks this reference system while encountering momentous changes in component values as well as time-varying disturbance.

V. SIMULATIONS

In this section, simulation results are presented in order to show the performance of the proposed NNs-based controller. The ducted fan UAV studied in its paper is numerically modeled and equipped with the proposed control strategy in Section IV. Dynamic system and its simulation are built and programed in MATLAB^{TM}. The relevant aerodynamic coefficients of the aircraft model are identified by CFD and functional-established by cubic spline interpolation. Then, three different simulations are conduct as follows:

A. SIMULATION 1: HOVER UNDER DISTURBANCE

In the first simulation, we intend to study the effect of parameter uncertainties on the dynamic response of proposed control scheme by verifying the fast convergence capacity of the ducted fan UAV in high-frequency disturbance condition. The aircraft is commanded to steadily hover at 10 meters' height and head to the north (i.e. yaw angle $\psi = 0$). Time-varying environmental wind disturbance, which is set as cosine function along Y_E axis with amplitude of 5m/s, is added to the dynamic model of the aircraft. Simulation results on roll channel under different control parameters are shown in Fig.8, including performance of angular velocity p and NN matching result for exogenous moment effect f_{21}.

In this simulation, taking consideration of simplicity, the basis function is chosen as $\mathbf{\Phi}_1 = [1]$, and the associated learning rate is then $\mathbf{\Gamma}_1 = \Gamma_1 I_{3\times3}$. The associated NN weight $\hat{W}_{11}$ is constrained into the compact set $\Omega_{11} = \{-3 \le \hat{W}_{11} \le 3\}$ by projection operator. Effect of exogenous moment f_{21} is the first component of $\mathbf{f}_2$ defined by (27). $\Gamma_{\mathbf{u}a1}$ is the first component of gain matrix $\mathbf{\Gamma}_{\mathbf{u}a}$ of the adaptive control input $\tilde{\mathbf{u}}_a$ defined by (34).

Fig.8 (a) shows the environmental disturbance act on the closed-loop system of the aircraft. Fig.8 (b) shows the performance of angular velocity p in counteracting this disturbance. In Fig.8 (b), the red dash curve marks the reference input x_{4d1}, which is the first component of $\mathbf{x}_{4d}$ defined by (25). This reference input is generated from the outer-loop of the controller. The black curve marks the system output merely acquired from the reference system without any influence of the NN controller. The green curve, brown curve, and blue curve mark the corresponding system output under different learning rates Γ_1 and adaptive gains $\Gamma_{\mathbf{u}c1}$. Fig.8 (c) shows the NN matching results for exogenous moment effect f_{21}. In Fig.8 (c), the red dash curve marks the real value of f_{21} which is calculated from the aircraft model. The green curve, brown curve, and blue curve mark the corresponding NN matching results under different parameters. Apparently, increasing the learning rate helps improve the performance for uncertainty identification of the proposed NNs, while the adaptive control input guarantees a competent robustness. It is seen from the blue curve in Fig.8 (c) that the NN weight $\hat{W}_{11}$ is limited to Ω_{11} as the learning rate Γ_1 increasing. As a result, we achieve an excellent and reliable NN matching ability for unknown terms. Consequently, shown in Fig.8 (b), as the disturbance identification and rejection ability being enhanced, performance for tracking certain reference input of the closed-loop system improves. This reveal an excellent performance and robustness of the proposed control scheme under parameter uncertainties.

B. SIMULATION 2: HOVER TO HIGH-SPEED TRANSITION

In the second simulation, we intend to give an overview of the hover to high-speed transition of the ducted fan UAV. Driven by a certain trajectory, the aircraft is commanded to accelerate at 2m/s^2 along X_E axis with altitude stabilized at 10m. This course is set to start at hover and end with horizontal velocity of 20m/s. Since the flight control strategy in Section IV ends up with velocity control, we introduce a simple feedback controller to generate the desired velocity commands along Y_E, Z_E axis. Thus, the complete driven trajectory is described by:

$$\begin{cases} x_{2d1} = \begin{cases} 2t, & x_{2d1} < x_{2d1f} \\ x_{2d1f}, & x_{2d1} = x_{2d1f} \end{cases} \\ x_{2d2} = -K_{p2}x_{12} \\ x_{2d3} = K_{p3}(x_{1d3} - x_{13}) \\ x_{3d3} = \bar{u}_{33} = 0 \end{cases} \tag{48}$$

where K_{p2} and K_{p3} are constant positive feedback gains. x_{2d1f} is the final horizontal velocity and x_{1d3} is the

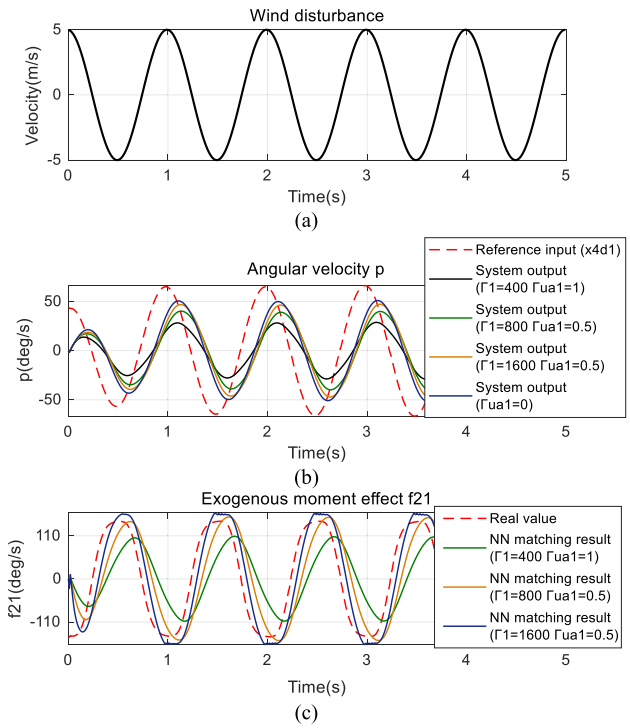

FIGURE 8. Results of simulation 1 on roll channel under different control parameters. (a) Disturbance. (b) Angular velocity. (c) Exogenous moment effect and its NN matching results.

desired altitude. In this simulation, $x_{2d1f} = 20m/s$ and $x_{1d3} = -10$. Moreover, the basis function vector is chosen as $\mathbf{\Phi}_1 = [\alpha_0 |V_E| \ \alpha_0^2 |V_E| \ \alpha_0 |V_E|^2 \ \alpha_0^2 |V_E|^2]^T$ whereas $|V_E| = \sqrt{u^2+v^2+w^2}$, $\cos\alpha_0 = -w/|V_E|$,and the associated learning rate is determined as $\mathbf{\Gamma}_1 = \text{diag}(2,2,0.1,0.1)$. It is worth pointing out that these basis functions are particularly determined based on the prior knowledge of $\mathbf{f}_2$ in order to reduce the neurons and show the effectiveness of the proposed method. For more accurate and reliable approximation results, more higher-order terms should be involved into $\mathbf{\Phi}_1$.

The corresponding simulation results are shown in Fig.9. Fig.9 (a)-(c) present the relevant system states during the transition. Throughout the whole process, the aircraft gradually heads down and continuously accelerates to the final velocity and adjusts itself to cruising flight at 20m/s. A more visualized result of the flight trajectory is presented in Fig.9 (d). Additionally, typical trajectories of NN weights are shown in Fig.9 (e)-(h). It is seen that NN weights adapt fast from 0s to 10s and quickly converge after 10s. This due to the fact that the flight data for NN training is not complete until 10s. After this time node, the transition is finished and the aircraft states are stabilized. Hence, as the NN is sufficiently trained, fast convergence for corresponding NN weights are then observed.

C. SIMULATION 3: TRANSITION UNDER DISTURBANCE AND NOISES

In the third simulation, we intend to verity the disturbance rejection ability of the proposed control scheme in the transition control. During this process, sine environmental wind disturbance with amplitude of 5m/s is invoked into the system. To simulate a real IMU sensing result, Gaussian noises are added into the measurements of angular velocity $\boldsymbol{\omega}$ and resultant force Υ in the body frame. The associated transition course is set to start at hover and end with horizontal

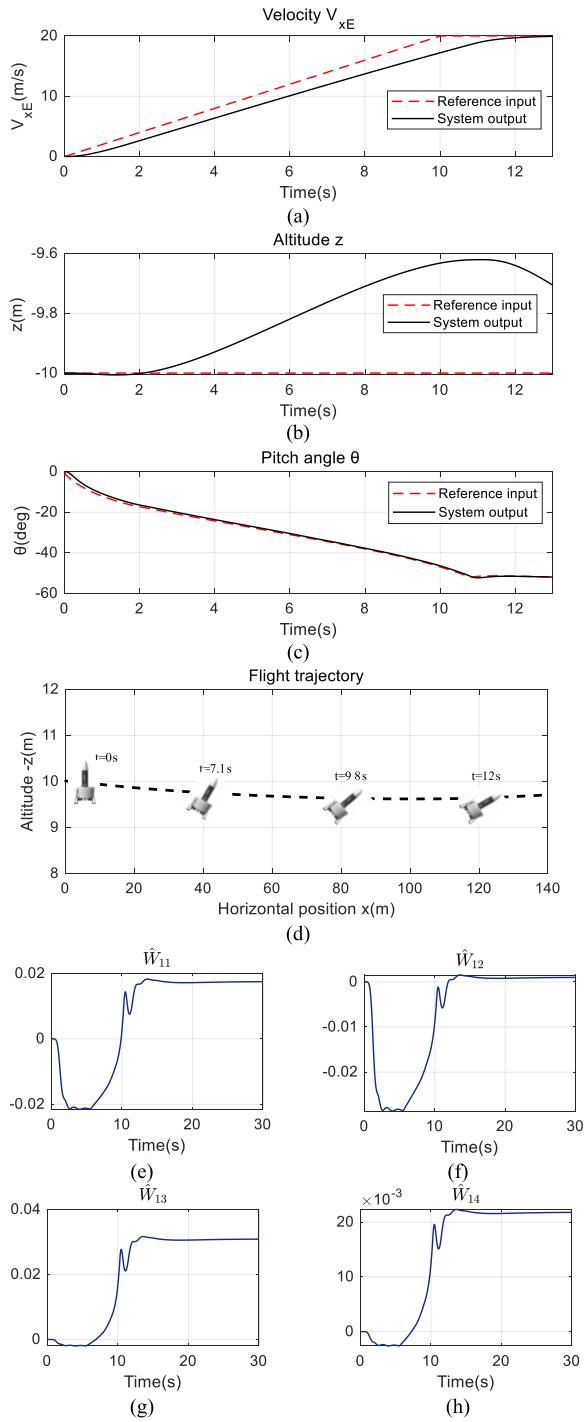

FIGURE 9. Results of simulation 2 for transition control. (a) Horizontal velocity. (b) Altitude. (c) Pitch angle. (d) Illustration of flight trajectory. (e)-(h) Trajectories of NN weights.

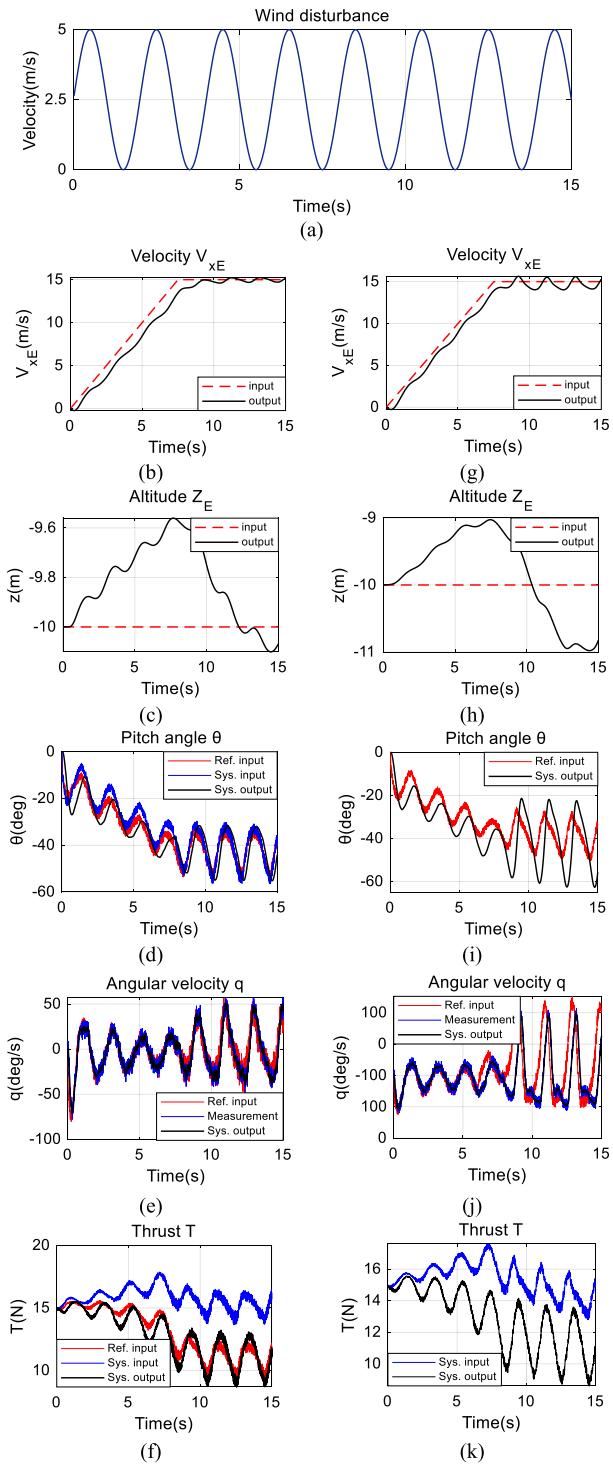

FIGURE 10. **Results of simulation 3 for transition control. (a) Wind disturbance. (b)-(f) Results from proposed method. (g)-(k) Results from method in [29].**

velocity of 15m/s. The driven trajectory is defined by (48) with final speed $x_{2d1f} = 15m/s$ and altitude $x_{1d3} = -10$.

Additionally, to show the advantage of the proposed NNs control scheme, we conduct a comparison between the proposed method and the adaptive method for tail-sitter UAV proposed in [29]. The main differences between these two methods are concluded as follows:

- We use NNs to estimate the uncertainties in this paper. While in [29], parameters for estimate the relevant uncertainties are designed based on the prior knowledge of the system model.
- The adaptive input in this paper is designed into a dynamic form to avoid adaptational actions in the denominator. While in [29], the adaptive control law is designed by a standard form with adaptive parameters occurred in the denominator.

The corresponding simulation results including more inner details about the NNs-based controller are shown in Fig.10. Fig.10 (a) shows the environmental disturbance act on the closed-loop system of the aircraft. Fig.10 (b)-(f) shows the transition control results of the proposed method, while the comparison results are given in Fig.10 (g)-(k). Fig.10 (b)(g) show the performance of horizontal velocity V_{xE}. In Fig.10 (b)(g), the red dash curve marks the reference input x_{2d1} and the black curve marks the system state $V_{xE} = x_{21}$. Fig.10 (c)(h) show the performance of altitude z. In Fig.10 (c)(h), the red dash curve marks the reference input -10 and black curve marks the system state $z = x_{13}$. The corresponding position feedback controller is defined by (48). Fig.10 (d)(i) show the performance of pitch Euler angle θ. In Fig.10 (d), the red curve marks the reference input which is the nominal attitude input $\bar{u}_{32}$ defined by (45), and the black curve marks the system state $\theta = x_{32}$. The blue curve marks the attitude input u_{32} of the outer-loop system defined by (37). Fig.10 (e)(j) show the performance of angular velocity q. In Fig.10 (e)(j), the red curve marks the reference input x_{4d2} and the black curve marks the system state $q = x_{42}$. The blue curve marks the corresponding measurement of the state with measurement noise. Fig.10 (f)(k) show the action of thrust. In Fig.10 (f), the red curve marks the reference input which is the nominal thrust input $\bar{u}_1$ defined by (45) and the black curve marks the actual thrust T. The blue curve marks the thrust input u_1 of the outer-loop system defined by (37).

According to the simulation results shown in Fig.10, the closed-loop system of the ducted fan reveals a good disturbance rejection performance. The aircraft is able to follow the desired trajectory to accomplish the hover to high-speed transition. Although suffering great changes on system values, the closed-loop system on attitude control (inner-loop) still exhibits a fast and accurate performance for tracking the reference signals, which is shown in Fig.10 (e). In the meanwhile, it is seen from Fig.10 (d)(f) that the adaptive inputs $\tilde{\mathbf{u}}_3$, $\tilde{u}_1$ of the outer-loop effectively compensate for the input uncertainties and make the actual input track the corresponding reference signals. Consequently, in strongly gusty environment, the aircraft's attitude and thrust is adjusted automatically to counteract the effect of wind disturbance. A good robustness of the closed-loop system is hence revealed.

Comparing the results of the proposed method (Fig.10 (b)-(f)) with the results of the adaptive method in [29]

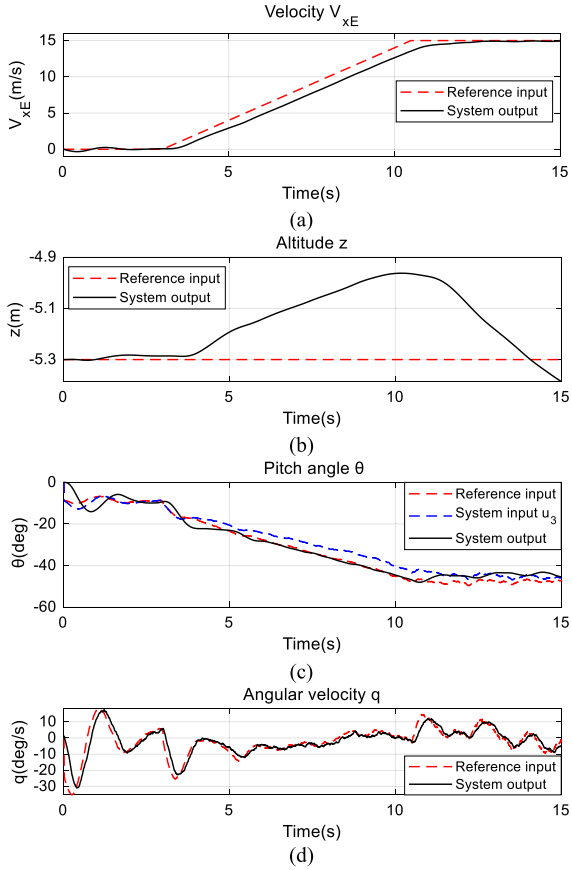

FIGURE 11. Flight test results for hover to high-speed transition. (a) Horizontal velocity. (b) Altitude. (c) Pitch angle. (d) Angular velocity.

(Fig.10 (g)-(k)), the advantage of the proposed NNs control scheme is obvious. Sever tracking errors of the attitude are observed at high-speed flight in Fig.10 (i)(j). This due to fact that the approximations of the uncertain terms $\mathbf{f}_2$ and $\mathbf{g}_2$ by the adaptive method are not accurate enough comparing with the NNs method in this paper. In the meanwhile, since there are no uncertainty compensations to the outer-loop in the adaptive method, horizontal velocity at high-speed in Fig.10 (g) suffers greater oscillations than that in Fig.10 (b). And the altitude loss of the adaptive method (Fig.10 (h)) is nearly double of that in the proposed method (Fig.10 (c)). Based on these results, we can conclude that the proposed NNs control scheme guarantees a more steady flight under disturbances and noises.

VI. FLIGHT TEST

In this section, experimental results are presented from practical flight tests (Fig.12). The ducted fan UAV studied in this paper is mounted with inertial measurement unit (IMU) and GPS to measure the relevant system states. Modules including data fusion, state estimation, communication and control scheme are coded into the airborne processor. The controller update and data download frequency is set as 100Hz. Taking environmental disturbance and flight safety

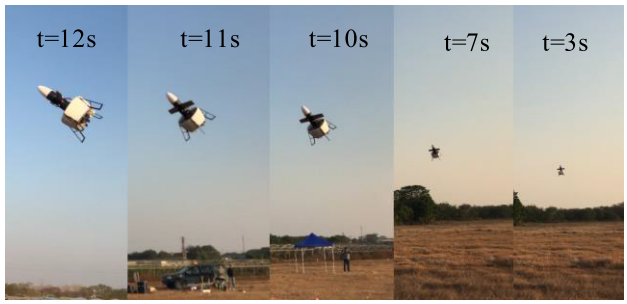

FIGURE 12. Flight test photographs.

into consideration, the transition course is set to start at hover and end with horizontal velocity of 15m/s, similar to that in simulation 3 in Section V. To implement the hover to high-speed transition, we first launch the aircraft and make it hover at an acceptable altitude. Then the driven trajectory defined by (48) with final speed of x_{2d1f} is sent to the airborne processor to control the aircraft accomplishing a transition process. In terms of implementation, we first choose a small final speed such as $x_{2d1f} = 5m/s$ to pre-train the neural networks. Convergent weights are set as initial values of the weights in the next move. Continue this step until the final speed gradually increases to the desired one $x_{2d1f} = 15m/s$. After that, the NNs are completely trained and a steady flight is then guaranteed.

The corresponding flight test results are shown in Fig.11, in which relevant definitions are similar to that in simulation 3. In Fig.11 (a), the red dash curve marks the reference input x_{2d1} and the black curve marks the system state $V_{xE} = x_{21}$. In Fig.11(b), the red dash curve marks the reference input -5.3 and black curve marks the system state $z = x_{13}$. In Fig.11 (c), the red dash curve marks the reference input $\bar{u}_{32}$ and the black curve marks the system state $\theta = x_{32}$. The blue dash curve marks the attitude input u_{32} of the outer-loop system. In Fig.11 (d), the red dash curve marks the reference input x_{4d2} and the black curve marks the system state $q = x_{42}$. It is seen in Fig.11 (b) that the actual altitude loss is less than 0.4m. Consistent with the simulation results in Section V, these flight test results demonstrate that the aircraft is capable to closely follow the mission trajectory.

VII. CONCLUSION

This paper concentrates on the transition control for hover to high-speed-level-flight of a ducted fan UAV. During this special process, nonlinearity and uncertainty of system values are emphasized as main issues. To tackle the problem, we propose a novel neural-networks-based controller that performs well in identifying uncertainties and tracking reference signals. In prior, key aerodynamic characteristics of the transition process are presented and analyzed. Then we model the dynamic system of the aircraft and reform it into a cascade underactuated nonlinear structure. In the meanwhile, the nominal controller design for nonlinear system based on neural networks is proposed and proved for stability.

Subsequently, the proposed control strategy is applied on the ducted fan model. As a result, the closed-loop system of the aircraft is capable of tracking a certain trajectory with desired dynamic performance. Three simulations are conduct in this paper. Simulation 1 shows a fast convergence capacity of the proposed NNs controller by hover experiments under high-frequency disturbance. In simulation 2 and 3 we exhibit the hover to high-speed transition, the results of which show a good robustness of the closed-loop system. Furthermore, this transition process is successfully performed by practice flight test. In all, we conclude that the proposed control scheme is feasible and effective.

APPENDIX A
PROJECTION OPERATOR

Definition A.1: Consider a convex compact set with a smooth boundary given by:

$$S_c = \{\boldsymbol{\theta} \in \mathbb{R}^n | f(\boldsymbol{\theta}) \leq c\}, \quad 0 \leq c \leq 1$$

where $f : \mathbb{R}^n \to \mathbb{R}$ is a smooth convex function given by:

$$f(\boldsymbol{\theta}) = \frac{(\varepsilon_0 + 1)\,\boldsymbol{\theta}^T\boldsymbol{\theta} - \boldsymbol{\theta}_{\max}^2}{\varepsilon_0 \boldsymbol{\theta}_{\max}^2}$$

with $\boldsymbol{\theta}_{\max}$ being the norm bound imposed on the vector $\boldsymbol{\theta}$, and $\varepsilon_0 > 0$ is the projection tolerance bound of our choice. The projection operator is defined as:

$$\mathrm{Proj}_{\Omega}(\boldsymbol{\theta}, \mathbf{y}) = \begin{cases} \mathbf{y} & \text{if } f(\boldsymbol{\theta}) < 0 \\ \mathbf{y} & \text{if } f(\boldsymbol{\theta}) \geq 0 \text{ and } \nabla f^T \mathbf{y} \leq 0 \\ \mathbf{y} - \dfrac{\nabla f}{\|\nabla f\|}\left\langle \dfrac{\nabla f}{\|\nabla f\|}, \mathbf{y} \right\rangle f(\boldsymbol{\theta}) & \\ & \text{if } f(\boldsymbol{\theta}) \geq 0 \text{ and } \nabla f^T \mathbf{y} > 0 \end{cases}$$

where $\Omega = S_1 = \{\boldsymbol{\theta} \in \mathbb{R}^n | f(\boldsymbol{\theta}) \leq 1\}$.

Property A.1: The projection operator does not alter $\mathbf{y}$ if $\boldsymbol{\theta}$ belongs to S_0. In the set $\{\boldsymbol{\theta} \in \mathbb{R}^n | 0 \leq f(\boldsymbol{\theta}) \leq 1\}$, if $\nabla f^T \mathbf{y} > 0$, the projection operator subtracts a vector normal to the boundary $\bar{\Omega}_{f(\boldsymbol{\theta})} = \{\boldsymbol{\theta} \in \mathbb{R}^n | f(\bar{\theta}) = f(\boldsymbol{\theta})\}$, so that we get a smooth transformation from the original vector filed $\mathbf{y}$ to an inward or tangent vector field for Ω [36].

Property A.2: Given the vectors $\mathbf{y} \in \mathbb{R}^n$, $\boldsymbol{\theta} \in \Omega$ and $\boldsymbol{\theta}^* \in S_0 \subset \Omega \subset R^n$ we have [36]:

$$\left(\boldsymbol{\theta} - \boldsymbol{\theta}^*\right)^T \left(\mathrm{Proj}_{\Omega}(\boldsymbol{\theta}, \mathbf{y}) - \mathbf{y}\right) \leq 0 \tag{49}$$

In this paper, we extend these definition and property to a matrix form.

Definition A.2: The projection operator of a matrix is defined as:

$$\mathbf{Proj}_{\Omega}(\boldsymbol{\Theta}, \mathbf{Y}) = \left[\, \mathrm{Proj}_{\Omega_1}(\boldsymbol{\theta}_1, \mathbf{y}_1) \quad \cdots \quad \mathrm{Proj}_{\Omega_m}(\boldsymbol{\theta}_m, \mathbf{y}_m) \,\right] \tag{50}$$

where $\boldsymbol{\Theta} = [\boldsymbol{\theta}_1 \ \cdots \ \boldsymbol{\theta}_m] \in \mathbb{R}^{n\times m}$ with $\boldsymbol{\theta}_i \in \Omega_i \subset \mathbb{R}^n$, and $\mathbf{y} = [y_1 \ \cdots \ y_m] \in \mathbb{R}^{n\times m}$, and $\Omega = \{\boldsymbol{\Theta} \in \mathbb{R}^{n\times m} | \boldsymbol{\theta}_i \in \Omega_i\}$.

Property A.3: Given the matrices $\mathbf{Y} \in \mathbb{R}^{n\times m}$, $\boldsymbol{\Theta} \in \mathbb{R}^{n\times m}$ with $\boldsymbol{\theta}_i \in \Omega_i$, and $\boldsymbol{\Theta}^* = \left[\boldsymbol{\theta}_1^* \ \cdots \ \boldsymbol{\theta}_m^*\right] \in R^{n\times m}$ with $\boldsymbol{\theta}_i^* \in S_0 \subset \Omega_i$, we have:

$$\mathrm{tr}\left[\left(\boldsymbol{\Theta} - \boldsymbol{\Theta}^*\right)^T \left(\mathbf{Proj}_{\Omega}(\boldsymbol{\Theta}, \mathbf{Y}) - \mathbf{Y}\right)\right] \leq 0 \tag{51}$$

APPENDIX B
PROOF OF THEOREM 1

For the nonlinear system (14), recall the parameterized system (19):

$$\dot{\mathbf{x}} = \left[\bar{\mathbf{f}}(\mathbf{x}) + \mathbf{W}_{\mathbf{f}}^T \boldsymbol{\Phi}_{\mathbf{f}}(\mathbf{x})\right] + \left[\bar{\mathbf{g}}(\mathbf{x}) + \mathbf{W}_{\mathbf{g}}^T \boldsymbol{\Phi}_{\mathbf{g}}(\mathbf{x})\right]\left(\bar{\mathbf{u}} + \tilde{\mathbf{u}}\right)$$

and the auxiliary system (22):

$$\begin{cases} \dot{\hat{\mathbf{x}}} = \bar{\mathbf{f}}(\mathbf{x}) + \hat{\mathbf{W}}_{\mathbf{f}}^T \boldsymbol{\Phi}_{\mathbf{f}} + \bar{\mathbf{g}}(\mathbf{x})\mathbf{u} + \hat{\mathbf{W}}_{\mathbf{g}}^T \boldsymbol{\Phi}_{\mathbf{g}}\mathbf{u} - \mathbf{K}_{\mathbf{x}}\left(\hat{\mathbf{x}} - \mathbf{x}\right) \\ \dot{\hat{\mathbf{W}}}_{\mathbf{f}} = \boldsymbol{\Gamma}_{\mathbf{f}}\mathbf{Proj}_{\Omega_{\mathbf{f}}}(\hat{\mathbf{W}}_{\mathbf{f}}, -\boldsymbol{\Phi}_{\mathbf{f}}\left(\hat{\mathbf{x}} - \mathbf{x}\right)^T) \\ \dot{\hat{\mathbf{W}}}_{\mathbf{g}} = \boldsymbol{\Gamma}_{\mathbf{g}}\mathbf{Proj}_{\Omega_{\mathbf{g}}}(\hat{\mathbf{W}}_{\mathbf{g}}, -\boldsymbol{\Phi}_{\mathbf{g}}\mathbf{u}\left(\hat{\mathbf{x}} - \mathbf{x}\right)^T) \end{cases}$$

Define the tracking error $\tilde{\mathbf{x}} = \hat{\mathbf{x}} - \mathbf{x}$, $\tilde{\mathbf{W}}_{\mathbf{f}} = \hat{\mathbf{W}}_{\mathbf{f}} - \mathbf{W}_{\mathbf{f}}$ and $\tilde{\mathbf{W}}_{\mathbf{g}} = \hat{\mathbf{W}}_{\mathbf{g}} - \mathbf{W}_{\mathbf{g}}$. Then, we can derive the error dynamics as:

$$\begin{cases} \dot{\tilde{\mathbf{x}}} = \tilde{\mathbf{W}}_{\mathbf{f}}^T \boldsymbol{\Phi}_{\mathbf{f}} + \tilde{\mathbf{W}}_{\mathbf{g}}^T \boldsymbol{\Phi}_{\mathbf{g}}\mathbf{u} - \mathbf{K}_{\mathbf{x}}\tilde{\mathbf{x}} \\ \dot{\tilde{\mathbf{W}}}_{\mathbf{f}} = \boldsymbol{\Gamma}_{\mathbf{f}}\mathbf{Proj}_{\Omega_{\mathbf{f}}}(\hat{\mathbf{W}}_{\mathbf{f}}, -\boldsymbol{\Phi}_{\mathbf{f}}\tilde{\mathbf{x}}^T) \\ \dot{\tilde{\mathbf{W}}}_{\mathbf{g}} = \boldsymbol{\Gamma}_{\mathbf{g}}\mathbf{Proj}_{\Omega_{\mathbf{g}}}(\hat{\mathbf{W}}_{\mathbf{g}}, -\boldsymbol{\Phi}_{\mathbf{g}}\mathbf{u}\tilde{\mathbf{x}}^T) \end{cases} \tag{52}$$

Consider the following Lyapunov function candidate:

$$V(t) = \frac{1}{2}\tilde{\mathbf{x}}^T\tilde{\mathbf{x}} + \frac{1}{2}\mathrm{tr}(\tilde{\mathbf{W}}_{\mathbf{f}}^T \boldsymbol{\Gamma}_{\mathbf{f}}^{-1}\tilde{\mathbf{W}}_{\mathbf{f}}) + \frac{1}{2}\mathrm{tr}(\tilde{\mathbf{W}}_{\mathbf{g}}^T \boldsymbol{\Gamma}_{\mathbf{g}}^{-1}\tilde{\mathbf{W}}_{\mathbf{g}}) \tag{53}$$

where tr denotes the trace of matrix. Apparently, $V(t) \geq 0$ as $\boldsymbol{\Gamma}_{\mathbf{f}}$, $\boldsymbol{\Gamma}_{\mathbf{g}}$ are positive definite diagonal matrices. Using *Property A.3* of projection operator, one can obtain:

$$\begin{cases} \tilde{\mathbf{W}}_{\mathbf{f}}^T\left[\boldsymbol{\Phi}_{\mathbf{f}}\tilde{\mathbf{x}}^T + \mathbf{Proj}_{\Omega_{\mathbf{f}}}(\hat{\mathbf{W}}_{\mathbf{f}}, -\boldsymbol{\Phi}_{\mathbf{f}}\tilde{\mathbf{x}}^T)\right] \leq 0 \\ \tilde{\mathbf{W}}_{\mathbf{g}}^T\left[\boldsymbol{\Phi}_{\mathbf{g}}\mathbf{u}\tilde{\mathbf{x}}^T + \mathbf{Proj}_{\Omega_{\mathbf{g}}}(\hat{\mathbf{W}}_{\mathbf{g}}, -\boldsymbol{\Phi}_{\mathbf{g}}\mathbf{u}\tilde{\mathbf{x}}^T)\right] \leq 0 \end{cases} \tag{54}$$

Then, we calculate the time derivative of the Lyapunov function along the trajectories of the system as:

$$\begin{aligned} \dot{V}(t) &= \tilde{\mathbf{x}}^T\dot{\tilde{\mathbf{x}}} + \mathrm{tr}(\tilde{\mathbf{W}}_{\mathbf{f}}^T \boldsymbol{\Gamma}_{\mathbf{f}}^{-1}\dot{\tilde{\mathbf{W}}}_{\mathbf{f}}) + \mathrm{tr}(\tilde{\mathbf{W}}_{\mathbf{g}}^T \boldsymbol{\Gamma}_{\mathbf{g}}^{-1}\dot{\tilde{\mathbf{W}}}_{\mathbf{g}}) \\ &= \tilde{\mathbf{x}}^T\left(\tilde{\mathbf{W}}_{\mathbf{f}}^T \boldsymbol{\Phi}_{\mathbf{f}} + \tilde{\mathbf{W}}_{\mathbf{g}}^T \boldsymbol{\Phi}_{\mathbf{g}}\mathbf{u} - \mathbf{K}_{\mathbf{x}}\tilde{\mathbf{x}}\right) \\ &\quad + \mathrm{tr}\left[\tilde{\mathbf{W}}_{\mathbf{f}}^T \boldsymbol{\Gamma}_{\mathbf{f}}^{-1}\boldsymbol{\Gamma}_{\mathbf{f}}\mathbf{Proj}_{\Omega_{\mathbf{f}}}(\hat{\mathbf{W}}_{\mathbf{f}}, -\boldsymbol{\Phi}_{\mathbf{f}}\tilde{\mathbf{x}}^T)\right] \\ &\quad + \mathrm{tr}\left[\tilde{\mathbf{W}}_{\mathbf{g}}^T \boldsymbol{\Gamma}_{\mathbf{g}}^{-1}\boldsymbol{\Gamma}_{\mathbf{g}}\mathbf{Proj}_{\Omega_{\mathbf{g}}}(\hat{\mathbf{W}}_{\mathbf{g}}, -\boldsymbol{\Phi}_{\mathbf{g}}\mathbf{u}\tilde{\mathbf{x}}^T)\right] \\ &= \left[\tilde{\mathbf{x}}^T\tilde{\mathbf{W}}_{\mathbf{f}}^T \boldsymbol{\Phi}_{\mathbf{f}}\right] + \left[\tilde{\mathbf{x}}^T\tilde{\mathbf{W}}_{\mathbf{g}}^T \boldsymbol{\Phi}_{\mathbf{g}}\mathbf{u}\right] - \tilde{\mathbf{x}}^T\mathbf{K}_{\mathbf{x}}\tilde{\mathbf{x}} \\ &\quad + \mathrm{tr}\left[\tilde{\mathbf{W}}_{\mathbf{f}}^T\mathbf{Proj}_{\Omega_{\mathbf{f}}}(\hat{\mathbf{W}}_{\mathbf{f}}, -\boldsymbol{\Phi}_{\mathbf{f}}\tilde{\mathbf{x}}^T)\right] \\ &\quad + \mathrm{tr}\left[\tilde{\mathbf{W}}_{\mathbf{g}}^T\mathbf{Proj}_{\Omega_{\mathbf{g}}}(\hat{\mathbf{W}}_{\mathbf{g}}, -\boldsymbol{\Phi}_{\mathbf{g}}\mathbf{u}\tilde{\mathbf{x}}^T)\right] \\ &= \mathrm{tr}(\boldsymbol{\Phi}_{\mathbf{f}}\tilde{\mathbf{x}}^T\tilde{\mathbf{W}}_{\mathbf{f}}^T) + \mathrm{tr}(\boldsymbol{\Phi}_{\mathbf{g}}\mathbf{u}\tilde{\mathbf{x}}^T\tilde{\mathbf{W}}_{\mathbf{g}}^T) - \tilde{\mathbf{x}}^T\mathbf{K}_{\mathbf{x}}\tilde{\mathbf{x}} \\ &\quad + \mathrm{tr}\left[\tilde{\mathbf{W}}_{\mathbf{f}}^T\mathbf{Proj}_{\Omega_{\mathbf{f}}}(\hat{\mathbf{W}}_{\mathbf{f}}, -\boldsymbol{\Phi}_{\mathbf{f}}\tilde{\mathbf{x}}^T)\right] \\ &\quad + \mathrm{tr}\left[\tilde{\mathbf{W}}_{\mathbf{g}}^T\mathbf{Proj}_{\Omega_{\mathbf{g}}}(\hat{\mathbf{W}}_{\mathbf{g}}, -\boldsymbol{\Phi}_{\mathbf{g}}\mathbf{u}\tilde{\mathbf{x}}^T)\right] \end{aligned}$$

$$
\begin{aligned}
&= \mathrm{tr}\left\{\tilde{\mathbf{W}}_{\mathbf{f}}^T\left[\mathbf{\Phi_f}\tilde{\mathbf{x}}^T + \mathbf{Proj}_{\Omega_{\mathbf{f}}}(\hat{\mathbf{W}}_{\mathbf{f}}, -\mathbf{\Phi_f}\tilde{\mathbf{x}}^T)\right]\right\} \\
&\quad + \mathrm{tr}\left\{\tilde{\mathbf{W}}_{\mathbf{g}}^T\left[\mathbf{\Phi_g}\mathbf{u}\tilde{\mathbf{x}}^T + \mathbf{Proj}_{\Omega_{\mathbf{g}}}(\hat{\mathbf{W}}_{\mathbf{g}}, -\mathbf{\Phi_g}\mathbf{u}\tilde{\mathbf{x}}^T)\right]\right\} \\
&\quad - \tilde{\mathbf{x}}^T\mathbf{K_x}\tilde{\mathbf{x}} \\
&= -\tilde{\mathbf{x}}^T\mathbf{K_x}\tilde{\mathbf{x}} \le 0
\end{aligned} \tag{55}
$$

This shows the stability in the sense of Lyapunov so that $\tilde{\mathbf{x}}$, $\tilde{\mathbf{W}}_{\mathbf{f}}$ and $\tilde{\mathbf{W}}_{\mathbf{g}}$ are bounded. Furthermore, we have:

$$
\begin{aligned}
\frac{1}{2}\left\|\tilde{\mathbf{x}}\right\|^2 \le V(t) \le V(0) \le \frac{1}{2}\lambda_{\max}(\mathbf{\Gamma_f}^{-1})\mathrm{tr}(\tilde{\mathbf{W}}_{\mathbf{f}}^T(0)\tilde{\mathbf{W}}_{\mathbf{f}}(0)) \\
+ \frac{1}{2}\lambda_{\max}(\mathbf{\Gamma_g}^{-1})\mathrm{tr}(\tilde{\mathbf{W}}_{\mathbf{g}}^T(0)\tilde{\mathbf{W}}_{\mathbf{g}}(0))
\end{aligned} \tag{56}
$$

where '$\lambda_{\max}$' denotes the maximum eigenvalue of matrix. The designed projection operators in (22) guarantee that $\hat{\mathbf{W}}_{\mathbf{f}} \in \Omega_{\mathbf{f}}$, $\hat{\mathbf{W}}_{\mathbf{g}} \in \Omega_{\mathbf{g}}$ [35]. Then according to *Definition A.1,* one can obtain:

$$
\begin{aligned}
&\frac{1}{2}\lambda_{\max}(\mathbf{\Gamma_f}^{-1})\mathrm{tr}(\tilde{\mathbf{W}}_{\mathbf{f}}^T(0)\tilde{\mathbf{W}}_{\mathbf{f}}(0)) \\
&\le \frac{1}{2}\lambda_{\max}(\mathbf{\Gamma_f}^{-1})\mathbf{W}_{\mathbf{f}\max}\frac{1}{2}\lambda_{\max}(\mathbf{\Gamma_g}^{-1})\mathrm{tr}(\tilde{\mathbf{W}}_{\mathbf{g}}^T(0)\tilde{\mathbf{W}}_{\mathbf{g}}(0)) \\
&\le \frac{1}{2}\lambda_{\max}(\mathbf{\Gamma_g}^{-1})\mathbf{W}_{\mathbf{g}\max}
\end{aligned} \tag{57}
$$

with

$$
\begin{aligned}
&\mathbf{W}_{\mathbf{f}\max}4\left(\mathbf{W}_{\mathbf{f}1\max}^2 + \mathbf{W}_{\mathbf{f}2\max}^2 + \cdots + \mathbf{W}_{\mathbf{f}n\max}^2\right) \\
&\mathbf{W}_{\mathbf{g}\max}4\left(\mathbf{W}_{\mathbf{g}1\max}^2 + \mathbf{W}_{\mathbf{g}2\max}^2 + \cdots + \mathbf{W}_{\mathbf{g}n\max}^2\right)
\end{aligned} \tag{58}
$$

where $\mathbf{W}_{\mathbf{f}i\max}, \mathbf{W}_{\mathbf{g}i\max}$ are the norm bounds of vectors $\mathbf{W}_{\mathbf{f}i}, \mathbf{W}_{\mathbf{g}i}$ defined by *Definition A.1* in Appendix A. Substituting (57), (58) into (56) we can obtain the bound of the prediction error $\tilde{\mathbf{x}}$:

$$
\left\|\tilde{\mathbf{x}}\right\|^2 \le \lambda_{\max}(\mathbf{\Gamma_f}^{-1})\mathbf{W}_{\mathbf{f}\max} + \lambda_{\max}(\mathbf{\Gamma_g}^{-1})\mathbf{W}_{\mathbf{g}\max} \tag{59}
$$

The second derivative of the Lyapunov function $V(t)$ is derived as:

$$
\ddot{V}(t) = -2\tilde{\mathbf{x}}^T\mathbf{K_x}\dot{\tilde{\mathbf{x}}} \tag{60}
$$

Recalling (52), the boundness of $\tilde{\mathbf{x}}$, $\tilde{\mathbf{W}}_{\mathbf{f}}$ and $\tilde{\mathbf{W}}_{\mathbf{g}}$ verifies the boundness of $\dot{\tilde{\mathbf{x}}}$ and hence of $\ddot{V}(t)$. This implies that $\dot{V}(t)$ is uniformly continuous. According to *Barbalat's Lemma*, we have $\lim_{t\to\infty}\dot{V}(t) = 0$, which leads to $\lim_{t\to\infty}\tilde{\mathbf{x}} = 0$. Since $\dot{\tilde{\mathbf{x}}}$ is uniformly continuous, the application of *Barbalat's Lemma* also gives us $\lim_{t\to\infty}\dot{\tilde{\mathbf{x}}} = 0$. Consequently, we can conclude that the states and dynamics of the auxiliary system converge to those of the original nonlinear system. This complete the proof.

APPENDIX C
PROOF OF THEOREM 2

Recall the parameterized system (19) with desired dynamic performance $\dot{\mathbf{x}}_m$(16):

$$
\begin{aligned}
\dot{\mathbf{x}} &= \dot{\mathbf{x}}_m + \mathbf{e} \\
\mathbf{e} &= \mathbf{W}_{\mathbf{f}}^T\mathbf{\Phi_f}(\mathbf{x}) + \bar{\mathbf{g}}(\mathbf{x})\tilde{\mathbf{u}} + \mathbf{W}_{\mathbf{g}}^T\mathbf{\Phi_g}(\mathbf{x})\mathbf{u} + \tilde{W}_{\mathbf{g}}^T\mathbf{\Phi_g}(\mathbf{x})\bar{\mathbf{u}}
\end{aligned} \tag{61}
$$

And the auxiliary system (22):

$$
\begin{cases}
\dot{\hat{\mathbf{x}}} = \dot{\mathbf{x}}_m + \hat{\mathbf{e}}(\tilde{\mathbf{u}}) - \mathbf{K_x}\tilde{\mathbf{x}} \\
\hat{\mathbf{e}}(\tilde{\mathbf{u}}) = \hat{\mathbf{W}}_{\mathbf{f}}^T\mathbf{\Phi_f} + \bar{\mathbf{g}}(\mathbf{x})\tilde{\mathbf{u}} + \hat{\mathbf{W}}_{\mathbf{g}}^T\mathbf{\Phi_g}\tilde{\mathbf{u}} + \hat{\mathbf{W}}_{\mathbf{g}}^T\mathbf{\Phi_g}\bar{\mathbf{u}} \\
\dot{\hat{\mathbf{W}}}_{\mathbf{f}} = \mathbf{\Gamma_f}\mathbf{Proj}_{\Omega_{\mathbf{f}}}(\hat{\mathbf{W}}_{\mathbf{f}}, -\mathbf{\Phi_f}(\mathbf{x})\left(\hat{\mathbf{x}} - \mathbf{x}\right)^T) \\
\dot{\hat{\mathbf{W}}}_{\mathbf{g}} = \mathbf{\Gamma_g}\mathbf{Proj}_{\Omega_{\mathbf{g}}}(\hat{\mathbf{W}}_{\mathbf{g}}, -\mathbf{\Phi_g}(\mathbf{x})\mathbf{u}\left(\hat{\mathbf{x}} - \mathbf{x}\right)^T)
\end{cases} \tag{62}
$$

Comparing (61) with (62), one obtain:

$$
\mathbf{e} = -\dot{\tilde{\mathbf{x}}} - \mathbf{K_x}\tilde{\mathbf{x}} + \hat{\mathbf{e}}(\tilde{\mathbf{u}}) \tag{63}
$$

According to *Theorem 1*, as $t \to \infty$, one has $\dot{\tilde{\mathbf{x}}} \to 0$ and $\tilde{\mathbf{x}} \to 0$. Therefore, $\mathbf{e} \to 0$ is equivalent to $\hat{\mathbf{e}} \to 0$. First, the time derivatives of $\hat{\mathbf{e}}$ along input $\tilde{\mathbf{u}}$ is derived as:

$$
\dot{\hat{\mathbf{e}}}(\tilde{\mathbf{u}}) = \left(\frac{\partial\hat{\mathbf{e}}}{\partial\tilde{\mathbf{u}}}\right)^T\dot{\tilde{\mathbf{u}}} = \left[\bar{\mathbf{g}}(\mathbf{x}) + \hat{\mathbf{W}}_{\mathbf{g}}^T\mathbf{\Phi_g}\right]\dot{\tilde{\mathbf{u}}} \tag{64}
$$

Consider the following Lyapunov function candidate:

$$
V(t) = \frac{1}{2}\hat{\mathbf{e}}^T\hat{\mathbf{e}} \ge 0 \tag{65}
$$

And subsequently we calculate the time derivative of the Lyapunov function:

$$
\dot{V}(t) = \hat{\mathbf{e}}^T\dot{\hat{\mathbf{e}}} = \hat{\mathbf{e}}^T\left[\bar{\mathbf{g}}(\mathbf{x}) + \hat{\mathbf{W}}_{\mathbf{g}}^T\mathbf{\Phi_g}\right]\dot{\tilde{\mathbf{u}}} \tag{66}
$$

Substituting (23) into (66) yields:

$$
\dot{V}(t) = -\hat{\mathbf{e}}^T\left[\bar{\mathbf{g}}(\mathbf{x}) + \hat{\mathbf{W}}_{\mathbf{g}}^T\mathbf{\Phi_g}\right]\mathbf{\Gamma_u}\left[\bar{\mathbf{g}}(\mathbf{x}) + \hat{\mathbf{W}}_{\mathbf{g}}^T\mathbf{\Phi_g}\right]^T\hat{\mathbf{e}} \le 0 \tag{67}
$$

Note that $\dot{V}(t) = 0$ if and only if $\hat{\mathbf{e}} = 0$. By Lyapunov theory, we can conclude that the equilibrium point $\hat{\mathbf{e}} = 0$ is asymptotically stable (i.e. $\lim_{t\to\infty}\hat{\mathbf{e}} = 0$), which is equivalent to $\mathbf{e} \to 0$ as aforementioned. This complete the proof.

APPENDIX D
PROOF OF THEOREM 3 AND THEOREM 4

Recalling the closed-loop system for (29) with control strategy of (31)(33)(34)(35), the second derivative of $\mathbf{x}_3$ is derived as:

$$
\begin{aligned}
\ddot{\mathbf{x}}_3 &= \frac{\mathrm{d}\left(\mathbf{Q}\mathbf{x}_4\right)}{\mathrm{d}t} \\
&= \mathbf{Q}\dot{\mathbf{x}}_4 + \left(\frac{\mathrm{d}\mathbf{Q}}{\mathrm{d}\mathbf{x}_3}\right)^T\Lambda\left(\dot{\mathbf{x}}_3\right)\mathbf{x}_4 \\
&= \mathbf{Q}\mathbf{g}_{2h}\mathbf{K}_4\left(\mathbf{Q}^{-1}\mathbf{K}_3\left(\mathbf{x}_{3d} - \mathbf{x}_3\right) - \mathbf{x}_4\right) + \mathbf{Q}\mathbf{e}_4 \\
&\quad - \mathbf{Q}\mathbf{g}_{2h}\mathbf{K}_4\left(\mathbf{g}_{2h}\mathbf{K}_4\right)^{-1}\mathbf{Q}^{-1}\left(\frac{\mathrm{d}\mathbf{Q}}{\mathrm{d}\mathbf{x}_3}\right)^T\Lambda\left(\mathbf{Q}\mathbf{x}_4\right)\mathbf{x}_4 \\
&\quad + \left(\frac{\mathrm{d}\mathbf{Q}}{\mathrm{d}\mathbf{x}_3}\right)^T\Lambda\left(\dot{\mathbf{x}}_3\right)\mathbf{x}_4 \\
&= \ddot{\mathbf{x}}_{3m} + \mathbf{Q}\mathbf{e}_4 \\
\mathbf{e}_4 &= \mathbf{W}_1^T\mathbf{\Phi}_1 + \mathbf{g}_{2h}\tilde{\mathbf{u}}_a + \mathbf{W}_2^T\mathbf{\Phi}_2\tilde{\mathbf{u}}_a + \mathbf{W}_2^T\mathbf{\Phi}_2\bar{\mathbf{u}}_a
\end{aligned} \tag{68}
$$

According to *Theorem 1* and *Theorem 2*, we have $\lim_{t\to\infty}\mathbf{e}_4 = 0$, which is equivalent to $\ddot{\mathbf{x}}_3 \to \ddot{\mathbf{x}}_{3m}$. Note that the expression of $\ddot{\mathbf{x}}_{3m}$ by (35) is a stable linear system.

Then the equilibrium point of $\mathbf{x_3}$ is resolved from $\ddot{\mathbf{x}}_{3m} = 0$, which is consequently $\mathbf{x_3} = \mathbf{x_{3d}}$. This complete the proof of *Theorem 3*.

Recalling the closed-loop system for (38) with control strategy of (39)(44)(45)(46)(47), substituting (45)(46) into (42) and recall the expression of $\mathbf{g}_1$ by (1), one obtain:

$$\dot{\mathbf{x}}_{2m} = \mathbf{a}_{2d} = \mathbf{K}_2(\mathbf{x}_{2d} - \mathbf{x}_2) \tag{69}$$

Let $\tilde{\mathbf{x}}_2 = \hat{\mathbf{x}}_2 - \mathbf{x}_2$, $\tilde{\mathbf{W}}_3 = \hat{\mathbf{W}}_3 - \mathbf{W}_3$. Then, we can derive the error dynamics as:

$$\begin{cases} \dot{\tilde{\mathbf{x}}}_2 = \tilde{\mathbf{g}}_1 \Xi(\Upsilon)\tilde{\mathbf{W}}_3^T \mathbf{\Phi}_3 - \mathbf{K}_{\mathbf{x}2}\tilde{\mathbf{x}}_2 \\ \dot{\tilde{\mathbf{W}}}_3 = \mathbf{\Gamma}_3 \mathbf{Proj}_{\Omega_3}\left[\hat{\mathbf{W}}_3, -\mathbf{\Phi}_3 \tilde{\mathbf{x}}_2^T \tilde{\mathbf{g}}_1 \Xi(\Upsilon_1)\right] \end{cases} \tag{70}$$

According to *Theorem 1*, we have $\tilde{\mathbf{x}}_2 \to 0, \dot{\tilde{\mathbf{x}}}_2 \to 0$. The time derivative of $\mathbf{x}_2$ is derived as:

$$\begin{aligned} \dot{\mathbf{x}}_2 &= (\dot{\mathbf{x}}_{2m} + \mathbf{e}_2) = \mathbf{K}_2(\mathbf{x}_{2d} - \mathbf{x}_2) + \mathbf{e}_2 \\ \mathbf{e}_2 &= -\dot{\tilde{\mathbf{x}}}_2 - \mathbf{K}_{\mathbf{x}2}\tilde{\mathbf{x}}_2 + \hat{\mathbf{e}}_2(\tilde{\mathbf{u}}_3, \tilde{u}_1) \\ \dot{\hat{\mathbf{e}}}_2 &= \left(\frac{\partial \hat{\mathbf{e}}_2}{\partial \tilde{\mathbf{u}}_3}\right)^T \dot{\tilde{\mathbf{u}}}_3 + \left(\frac{\partial \hat{\mathbf{e}}_2}{\partial u_1}\right)^T \dot{\tilde{u}}_1 \\ &= \tilde{\mathbf{g}}_1 \Xi(\Upsilon)\dot{\tilde{\mathbf{u}}}_3 + \bar{\mathbf{g}}_1 \begin{bmatrix} 0 & 0 & 1 \end{bmatrix}^T \dot{\tilde{u}}_1 \end{aligned} \tag{71}$$

According to *Theorem 2*, we have $\lim_{t\to\infty} \mathbf{e}_2 = 0$, which leads to $\dot{\mathbf{x}}_2 \to \dot{\mathbf{x}}_{2m}$. Note that linear system $\dot{\mathbf{x}}_{2m}$ is asymptotically stable. Then equilibrium point of $\mathbf{x}_2$ is resolved from $\dot{\mathbf{x}}_{2m} = 0$, which is consequently $\mathbf{x}_2 = \mathbf{x}_{2d}$. This complete the proof of *Theorem 4*.

REFERENCES

[1] J. Fleming, T. Jones, W. Ng, P. Gelhausen, and D. Enns, "Improving control system effectiveness for ducted fan VTOL UAVs operating in crosswinds," in *Proc. 2nd AIAA Unmanned Unlimited Conf. Workshop Exhib.* San Diego, CA, USA: AIAA, 2003, Sep. 2003.

[2] J. M. Pflimlin, P. Soueres, and T. Hamel, "Position control of a ducted fan VTOL UAV in crosswind," *Int. J. Control*, vol. 80, no. 5, pp. 666–683, May 2007.

[3] E. N. Johnson and M. A. Turbe, "Modeling, control, and flight testing of a small ducted-fan aircraft," *J. Guid. Control Dyn.*, vol. 29, no. 4, pp. 769–779, Jul./Aug. 2006.

[4] J. M. Pflimlin, P. Binetti, D. Trouchet, P. Soueres, and T. Hamel, "Aerodynamic modeling and practical attitude stabilization of a ducted fan UAV," in *Proc. Eur. Control Conf. (ECC)*, Jul. 2007, pp. 4023–4029.

[5] A. Manouchehri, H. Hajkarami, and M. S. Ahmadi, "Hovering control of a ducted fan VTOL unmanned aerial vehicle (UAV) based on PID control," in *Proc. Int. Conf. Electr. Control Eng.*, Sep. 2011, pp. 5962–5965.

[6] I. K. Peddle, T. Jones, and J. Treurnicht, "Practical near hover flight control of a ducted fan (SLADe)," *Control Eng. Pract.*, vol. 17, no. 1, pp. 48–58, Jan. 2009.

[7] L. Marconi, R. Naldi, and L. Gentili, "Modelling and control of a flying robot interacting with the environment," *Automatica*, vol. 47, no. 12, pp. 2571–2583, Dec. 2011.

[8] A. Roberts and A. Tayebi, "Adaptive position tracking of VTOL UAVs," *IEEE Trans. Robot.*, vol. 27, no. 1, pp. 129–142, Feb. 2011.

[9] S. Sheng and C. Sun, "A near-hover adaptive attitude control strategy of a ducted fan micro aerial vehicle with actuator dynamics," *Appl. Sci.*, vol. 5, no. 4, pp. 666–681, Sep. 2015.

[10] S. A. Emami and A. Rezaeizadeh, "Adaptive model predictive control-based attitude and trajectory tracking of a VTOL aircraft," *IET Control Appl.*, vol. 12, no. 15, pp. 2031–2042, Oct. 2018.

[11] Y. Jung and D. H. Shim, "Development and application of controller for transition flight of tail-sitter UAV," *J. Intell. Robotic Syst.*, vol. 65, nos. 1–4, pp. 137–152, Jan. 2012.

[12] Y. Jung, S. Cho, and D. H. Shim, "A comprehensive flight control design and experiment of a tail-sitter UAV," in *Proc. AIAA Guid., Navigat., Control (GNC) Conf.*, Aug. 2013, p. 4992.

[13] H. Liu, F. Peng, F. L. Lewis, and Y. Wan, "Robust tracking control for tail-sitters in flight mode transitions," *IEEE Trans. Aerosp. Electron. Syst.*, vol. 55, no. 4, pp. 2023–2035, Aug. 2019.

[14] V. Artale, M. Collotta, C. Milazzo, G. Pau, and A. Ricciardello, "An integrated system for UAV control using a neural network implemented in a prototyping board," *J. Intell. Robotic Syst.*, vol. 84, nos. 1–4, pp. 5–19, Dec. 2016.

[15] H. M. Guzey, T. Dierks, S. Jagannathan, and L. Acar, "Modified consensus-based output feedback control of quadrotor UAV formations using neural networks," *J. Intell. Robotic Syst.*, vol. 94, no. 1, pp. 283–300, Apr. 2019.

[16] C. Rosales, C. M. Soria, and F. G. Rossomando, "Identification and adaptive PID control of a hexacopter UAV based on neural networks," *Int. J. Adapt. Control Signal Process.*, vol. 33, no. 1, pp. 74–91, Jan. 2019.

[17] D. Ding, Z. Wang, Q.-L. Han, and G. Wei, "Neural-network-based output-feedback control under round-robin scheduling protocols," *IEEE Trans. Cybern.*, vol. 49, no. 6, pp. 2372–2384, Jun. 2019.

[18] J. Muliadi and B. Kusumoputro, "Neural network control system of UAV altitude dynamics and its comparison with the PID control system," *J. Adv. Transp.*, vol. 2018, pp. 1–18, 2018.3823201

[19] T. Dierks and S. Jagannathan, "Output feedback control of a quadrotor UAV using neural networks," *IEEE Trans. Neural Netw.*, vol. 21, no. 1, pp. 50–66, Jan. 2010.

[20] G. Lai, Z. Liu, Y. Zhang, and C. L. P. Chen, "Adaptive position/attitude tracking control of aerial robot with unknown inertial matrix based on a new robust neural identifier," *IEEE Trans. Neural Netw. Learn. Syst.*, vol. 27, no. 1, pp. 18–31, Jan. 2016.

[21] F. Jiang, F. Pourpanah, and Q. Hao, "Design, implementation, and evaluation of a neural-network-based quadcopter UAV system," *IEEE Trans. Ind. Electron.*, vol. 67, no. 3, pp. 2076–2085, Mar. 2020.

[22] H. Modares, F. L. Lewis, and M.-B. Naghibi-Sistani, "Adaptive optimal control of unknown constrained-input systems using policy iteration and neural networks," *IEEE Trans. Neural Netw. Learn. Syst.*, vol. 24, no. 10, pp. 1513–1525, Oct. 2013.

[23] S.-L. Dai, M. Wang, and C. Wang, "Neural learning control of marine surface vessels with guaranteed transient tracking performance," *IEEE Trans. Ind. Electron.*, vol. 63, no. 3, pp. 1717–1727, Mar. 2016.

[24] B. Xu, D. Wang, Y. Zhang, and Z. Shi, "DOB-based neural control of flexible hypersonic flight vehicle considering wind effects," *IEEE Trans. Ind. Electron.*, vol. 64, no. 11, pp. 8676–8685, Nov. 2017.

[25] B. S. Kim and S. J. Yoo, "Approximation-based adaptive control of uncertain non-linear pure-feedback systems with full state constraints," *IET Control Theory Appl.*, vol. 8, no. 17, pp. 2070–2081, Nov. 2014.

[26] L. Liu, D. Wang, Z. Peng, and H. H. T. Liu, "Saturated coordinated control of multiple underactuated unmanned surface vehicles over a closed curve," *Sci. China Inf. Sci.*, vol. 60, no. 7, Jul. 2017, Art. no. 070203.

[27] D. Xu, J. Huang, X. Su, and P. Shi, "Adaptive command-filtered fuzzy backstepping control for linear induction motor with unknown end effect," *Inf. Sci.*, vol. 477, pp. 118–131, Mar. 2019.

[28] T. Zhao, Y. Liu, Z. Li, C.-Y. Su, and Y. Feng, "Adaptive control and optimization of mobile manipulation subject to input saturation and switching constraints," *IEEE Trans. Autom. Sci. Eng.*, vol. 16, no. 4, pp. 1543–1555, Oct. 2019.

[29] W. Wang, J. Zhu, M. Kuang, and X. Zhu, "Adaptive attitude control for a tail-sitter UAV with single thrust-vectored propeller," in *Proc. IEEE Int. Conf. Robot. Autom. (ICRA)*, May 2018, pp. 6581–6586.

[30] C. Chen, T. T. Dong, W. J. Fu, and N. Liu, "On dynamic characteristics and stability analysis of the ducted fan unmanned aerial vehicles," *Int. J. Adv. Robotic Syst.*, vol. 16, no. 4, Jul. 2019, Art. no. 1729881419867018.

[31] B. Stiltner and O. Ohanian, "Fan angular momentum analysis for ducted fan UAVs during conceptual design," in *Proc. 50th AIAA Aerosp. Sci. Meeting Including New Horizons Forum Aerosp. Exposit.*, Jan. 2012, p. 852.

[32] W. Graf, J. Fleming, and W. Ng, "Improving ducted fan UAV aerodynamics in forward flight," in *Proc. 46th AIAA Aerosp. Sci. Meeting Exhib.*, 2008, p. 430.

[33] Y. Zhang, C. Xiang, and B. Xu, "Modeling and comprehensive analysis of an innovative coaxial ducted fan aircraft," in *Proc. Int. Conf. Adv. Mech. Syst. (ICAMechS)*, Aug. 2018, pp. 78–85.

[34] O. Ohanian, P. Gelhausen, and D. Inman, "A compact method for modeling the aerodynamics of ducted fan vehicles," in *Proc. 48th AIAA Aerosp. Sci. Meeting Including New Horizons Forum Aerosp. Exposit.*, Jan. 2010, p. 1052.

[35] Y. Zhang, S. Li, and X. Liu, "Adaptive near-optimal control of uncertain systems with application to underactuated surface vessels," *IEEE Trans. Control Syst. Technol.*, vol. 26, no. 4, pp. 1204–1218, Jul. 2018.

[36] J.-B. Pomet and L. Praly, "Adaptive nonlinear regulation: Estimation from the Lyapunov equation," *IEEE Trans. Autom. Control*, vol. 37, no. 6, pp. 729–740, Jun. 1992.

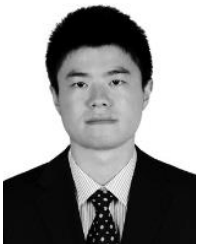

ZIHUAN CHENG received the B.S. degree in aeronautic science and engineering from the Beijing University of Aeronautics and Astronautics. He is currently pursuing the Ph.D. degree with the School of Automation Science and Engineering, South China University of Technology, Guangzhou, China.

His research interests include aerodynamic design and analysis, nonlinear systems, neural networks, and aircraft control.

HAILONG PEI (Member, IEEE) was born in 1965. He received the Ph.D. degree in automatic control from the South China University of Technology, Guangzhou, China, in 1992.

From 1997 to 1998, he did a Postdoctoral Research in The Chinese University of Hong Kong. He is currently a Professor with the School of Automation Science and Engineering, South China University of Technology, Guangzhou, China. His research interests include robot control, neural networks, nonlinear control, and so on.

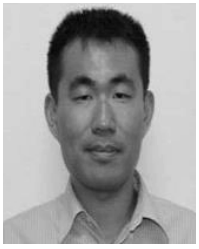

SHUAI LI (Member, IEEE) received the B.E. degree in precision mechanical engineering from the Hefei University of Technology, China, in 2005, the M.E. degree in automatic control engineering from the University of Science and Technology of China, China, in 2008, and the Ph.D. degree in electrical and computer engineering from the Stevens Institute of Technology, USA, in 2014. He is currently an Associate Professor (Reader) with the School of Engineering, Swansea University, Swansea, U.K.

His current research interests include dynamic neural networks, robotic networks, and other dynamic problems defined on a graph.